



The Luminosity Phase Space of Galactic and Extragalactic X-Ray Transients Out to Intermediate Redshifts

Ava Polzin¹ , Raffaella Margutti^{2,3} , Deanne L. Coppejans^{4,5} , Katie Auchetti^{6,7,8} , Kim L. Page⁹ , Georgios Vasilopoulos^{10,11,12} , Joe S. Bright¹³ , Paolo Esposito^{14,15} , Peter K. G. Williams^{16,17} , Koji Mukai^{18,19} , and Edo Berger¹⁶

¹ Department of Astronomy and Astrophysics, The University of Chicago, Chicago, IL 60637, USA; apolzin@uchicago.edu

² Department of Astronomy, University of California, Berkeley, CA 94720, USA

³ Department of Physics, University of California, Berkeley, CA 94720, USA

⁴ Department of Physics, University of Warwick, Gibbet Hill Road, Coventry CV4 7AL, UK

⁵ Department of Physics & Astronomy and Center for Interdisciplinary Exploration and Research in Astrophysics, Northwestern University, Evanston, IL 60208, USA

⁶ School of Physics, The University of Melbourne, Parkville, VIC 3010, Australia

⁷ ARC Centre of Excellence for All Sky Astrophysics in 3 Dimensions (ASTRO 3D), Australia

⁸ Department of Astronomy and Astrophysics, University of California, Santa Cruz, CA 95064, USA

⁹ School of Physics & Astronomy, University of Leicester, Leicester LE1 7RH, UK

¹⁰ Université de Strasbourg, CNRS, Observatoire astronomique de Strasbourg, UMR 7550, F-67000 Strasbourg, France

¹¹ Department of Physics, National and Kapodistrian University of Athens, University Campus Zografos, GR 15784, Athens, Greece

¹² Institute of Accelerating Systems & Applications, University Campus Zografos, Athens, Greece

¹³ Astrophysics, Department of Physics, University of Oxford, Keble Road, Oxford OX1 3RH, UK

¹⁴ Scuola Universitaria Superiore IUSS Pavia, Palazzo del Broletto, piazza della Vittoria 15, I-27100 Pavia, Italy

¹⁵ INAF—Istituto di Astrofisica Spaziale e Fisica Cosmica di Milano, Via A. Corti 12, I-20133 Milano, Italy

¹⁶ Center for Astrophysics | Harvard & Smithsonian, 60 Garden Street, Cambridge, MA 02138-1516, USA

¹⁷ American Astronomical Society, 1667 K Street NW, Suite 8006, Washington, DC 20006, USA

¹⁸ CRESST II and X-ray Astrophysics Laboratory, NASA/GSFC, Greenbelt, MD 20771, USA

¹⁹ Department of Physics, University of Maryland, Baltimore County, 1000 Hilltop Circle, Baltimore, MD 21250, USA

Received 2022 November 7; revised 2023 September 2; accepted 2023 September 5; published 2023 December 7

Abstract

We present a detailed compilation and analysis of the X-ray phase space of low- to intermediate-redshift ($0 \leq z \leq 1$) transients that consolidates observed light curves (and theory where necessary) for a large variety of classes of transient/variable phenomena in the 0.3–10 keV energy band. We include gamma-ray burst afterglows, supernovae, supernova shock breakouts and shocks interacting with the environment, tidal disruption events and active galactic nuclei, fast blue optical transients, cataclysmic variables, magnetar flares/outbursts and fast radio bursts, cool stellar flares, X-ray binary outbursts, and ultraluminous X-ray sources. Our overarching goal is to offer a comprehensive resource for the examination of these ephemeral events, extending the X-ray duration–luminosity phase space (DLPS) to show luminosity evolution. We use existing observations (both targeted and serendipitous) to characterize the behavior of various transient/variable populations. Contextualizing transient signals in the larger DLPS serves two primary purposes: to identify areas of interest (i.e., regions in the parameter space where one would expect detections, but in which observations have historically been lacking), and to provide initial qualitative guidance in classifying newly discovered transient signals. We find that while the most luminous (largely extragalactic) and least luminous (largely Galactic) part of the phase space is well populated at $t > 0.1$ days, intermediate-luminosity phenomena ($L_X = 10^{34}–10^{42}$ erg s^{−1}) represent a gap in the phase space. We thus identify $L_X = 10^{34}–10^{42}$ erg s^{−1} and $t = 10^{-4}$ to 0.1 days as a key discovery phase space in transient X-ray astronomy.

Unified Astronomy Thesaurus concepts: X-ray astronomy (1810); X-ray telescopes (1825); X-ray transient sources (1852); High energy astrophysics (739); Transient sources (1851); Time domain astronomy (2109)

1. Introduction

Transient and variable electromagnetic emission is often associated with the most violent events in space, like stellar explosions, stellar disruptions by supermassive black holes, or accretion-related phenomena on compact objects, to name a few. Studying the timescales and intrinsic energy released by each of these phenomena often provides guidance to understand the physics that regulates the bright displays of these transients and variables. To this end, the duration–luminosity phase space

(DLPS), where duration is defined as the time between the identification of an outburst and its later nondetection, has been used as a means of placing classes of transient and variable phenomena in the context of their underlying physics and constraining their outburst mechanisms.

Previous works have focused on building an observationally motivated, light-curve-populated DLPS for specific wavelength regimes (e.g., optical wavelengths, Kulkarni 2012; Pietka et al. 2015; Villar et al. 2017; millimeter wavelengths, Eftekhari et al. 2022; radio wavelengths, Metzger et al. 2015), which is facilitated by the significant volume of available data. We build on the first attempts to produce an observation-driven DLPS in the X-rays (Soderberg et al. 2009; O’Brien & Smartt 2013) by populating the DLPS with light curves as a comprehensive

view of the low-to-intermediate-redshift ($z \leq 1$, in order to ensure that the sample of sources in the DLPS is representative of the overall demographics presented and that the intrinsic rate of such events is well understood) phase space for (observer-frame) 0.3–10 keV transient and variable X-ray phenomena. This extends the use of the DLPS by showing both the luminosity and time evolution of these events. The motivation behind compiling this data set is two-pronged: to identify pristine regions of this parameter space that can be explored by future observing facilities (i.e., identification of discovery areas), and conversely, we can use the phase-space location of an unknown type of transient to constrain its intrinsic nature. This dual motivation, both for characterizing the nature of observed events and for identifying discovery frontiers for the future generation of X-ray observatories, makes examination of the phase space vital.

With a number of large-scale, all-sky transient surveys that have been carried out at the time of writing (e.g., SRG/eROSITA; Predehl et al. 2021) or are beginning in the immediate future, the DLPS can offer an initial rapid designation for observed events in tandem with targeted follow-up or before follow-up is initiated. The DLPS is also a resource for retroactive classification of transients recovered from archival data, when follow-up is potentially no longer possible, making it a valuable tool to determine object class from existing observations.

We utilize complete X-ray light curves for a variety of Galactic and extragalactic transient and variable phenomena: gamma-ray burst (GRB) afterglows, supernovae (SNe), SN shock breakouts (SBOs) and shocks interacting with the environment, tidal disruption events (TDEs) and active galactic nuclei (AGNs), fast blue optical transients (FBOTs), cataclysmic variables (CVs), magnetar flares/outbursts and fast radio bursts (FRBs), cool stellar flares, X-ray binary (XRB) outbursts, and ultraluminous X-ray sources (ULXs). For some classes the data are sparse, and we will instead plot peak X-ray luminosity (L_X) versus duration. In the one case where there were insufficient (*confirmed*) observations, we used theory as a supplement.

We present in Section 2 the data sets for each of the different classes of transient and variable events, and we discuss their location within the DLPS. In Section 3, we examine the use cases for our comprehensive DLPS. Where available, redshifts were used to correct the duration to the rest frame and to determine the luminosity distance, assuming a cosmology with $H_0 = 69.6 \text{ km s}^{-1} \text{ Mpc}^{-1}$, $\Omega_M = 0.286$, and $\Omega_\Lambda = 0.714$.

2. Data

We assembled X-ray data from a variety of sources. For ease and readability, we include lists of events, as well as their classifications, coordinates, distances, and the relevant literature in Appendix A. Light-curve data used in this paper are available on GitHub²⁰ and in a Zenodo repository at doi:10.5281/zenodo.8319602. In Sections 2.1–2.9, we briefly define each (sub)class of transient/variable, describe their characteristic timescale and luminosity as inferred from their position in the DLPS, and detail the provenance of the light-curve data used in this work (summarized in Table 1).

For transient classes—i.e., events that cannot repeat in the same astrophysical object—the light curves are from pointed

observations acquired after the detection/identification of the transient. As a result, only a subset of the observations capture the peak X-ray luminosity. The situation is somewhat different for variable light curves, some of which include data taken while monitoring the source. We expect that only a fraction of these light curves come from serendipitous detections owing to the small field of view (FOV) of the available X-ray instruments.

These data are used in the observational DLPS (Figure 1), where they show the luminosity evolution of observed light curves with time. These same data are used to calculate important X-ray quantities like peak L_X and isotropic equivalent energy, shown in Figure 2, where clustering by class remains apparent. These summary properties provide a means to characterize the light curves regardless of which stage of outburst they cover.

2.1. Gamma-Ray Burst Afterglows

GRBs (Table A1) are bursts of γ -rays associated with either the collapse of a massive star (GRBs with a duration of the γ -ray emission $T_{90} > 2 \text{ s}$) or the merger of compact objects (i.e., neutron stars and black holes). All GRB X-ray afterglow data shown in Figure 3 were collected via the UK Swift Science Data Centre²¹ (Evans et al. 2007, 2009), with the notable exceptions of the pre-Swift-era subluminal GRBs, GRB 980425A (Pian et al. 2000; Kouveliotou et al. 2004) and GRB 031203A (Sazonov et al. 2004; Watson et al. 2004). We include long GRBs (IGRBs), short GRBs (sGRBs), ultralong GRBs, and subluminal GRBs for $z \leq 1$ in our plotted population where redshift information is available.²² We also include the X-ray afterglow counterpart of the neutron star merger event GW170817, for which gravitational-wave emission was detected (e.g., Abbott et al. 2017; Hajela et al. 2019, 2020; Nakar 2020; Margutti & Chornock 2021). We excluded GRBs without well-constrained redshifts, as we are interested in luminosity versus intrinsic duration (rather than fluence vs. observed duration).

Our sample is complete for subluminal and ultralong GRBs. We include all but one of the long GRBs within $z = 1$ with X-ray observations from the end of 2014 through 2019 December and all but one of the X-ray observations of short GRBs within $z = 1$ from 2005 through 2017.

Differentiation of the subclasses of GRBs was informed by the T_{90} parameter (i.e., the time interval over which 90% of the γ -ray emission is observed). Short GRBs typically have $T_{90} < 2 \text{ s}$, long GRBs fall within the $2\text{--}10^3 \text{ s}$ range (Kouveliotou et al. 1993), and ultralong GRBs have T_{90} between 10^3 and 10^4 s (Levan et al. 2014). We note that some subluminal GRBs, while having a duration similar to that of long or ultralong GRBs, might actually represent physically distinct phenomena (e.g., SN SBOs; see Section 2.2) with $L_X \lesssim 10^{47} \text{ erg s}^{-1}$ (Norris 2003).

2.2. Explosion Shock Breakouts

SBOs (Table A2) are the emergence of the first (observable) photons from a stellar explosion. An SBO occurs as the shock goes through the star and reaches an optical depth of $\tau \sim c/v_{\text{shock}}$ within the star or at the stellar surface or in the stellar wind. Short-duration energetic emission is observable in the X-rays if the shock breaks out from a compact progenitor

²⁰ <https://github.com/avapolzin/X-rayLCs>; we also include some plotting and preliminary light-curve classification helper scripts in this repository.

²¹ <https://www.swift.ac.uk>

²² <https://www.mpe.mpg.de/~jcg/grbgen.html>

Table 1
Summary of the Classes and Subclasses (If Any) of Transients Included in This Work

Class, N	Subclass, N	Observatories
Gamma-ray bursts (GRBs), 52	Short GRBs (sGRBs), 19	Swift, BeppoSAX, Chandra, XMM-Newton
	Long GRBs (lGRBs), 25	Swift, Chandra
	Ultralong GRBs, 2	Swift
	Subluminous GRBs, 6	Swift, BeppoSAX, Chandra, XMM-Newton
	Wind SBO, 1	Swift
Shock breakouts (SBOs), 1 (+6) ^a	(Stellar surface SBOs, 6)	(Swift, BeppoSAX, Chandra, XMM-Newton)
Supernovae (SNe), 35	Type I core-collapse, 9	Swift, BeppoSAX, Chandra, XMM-Newton, ASCA, ROSAT
	Type II core-collapse, 13	Swift, Chandra, XMM-Newton, ASCA
	Interacting SNe, 9	Swift, BeppoSAX, Chandra, XMM-Newton, ASCA, ROSAT
	Superluminous SNe (SLSNe), 2	Swift, Chandra
	Ca-rich SNe, 2	Swift, Chandra
Tidal disruption events (TDEs), 19	Thermal TDEs, 16	Swift, Chandra, XMM-Newton, ROSAT
	Nonthermal TDEs, 3	Swift, Chandra, XMM-Newton, ROSAT
		Chandra, XMM-Newton
Active galactic nuclei (AGNs), 8		Swift, Chandra, XMM-Newton, eROSITA
Fast blue optical transients (FBOTs), 5		Swift, BeppoSAX, XMM-Newton, ASCA, ROSAT, RXTE
Cataclysmic variables (CVs), 41	Novae, 38	Swift, BeppoSAX, XMM-Newton, ASCA, ROSAT, RXTE
	Dwarf novae, 3	Swift, RXTE
Magnetar flares/outbursts, 15	Outburst, 14	Swift, BeppoSAX, Chandra XMM-Newton, ASCA, ROSAT, RXTE, MAXI
	Intermediate flare/short burst, 1	Swift, MAXI
		Insight-HXMT
Fast radio bursts (FRBs), 1		XMM-Newton
Cool stellar flares, 18		Swift, Chandra, XMM-Newton, RXTE, eROSITA, NICER
X-ray binary outbursts (XRBs), 17	Low-mass XRBs (LMXRBs), 4	Swift, Chandra, XMM-Newton, RXTE
	High-mass XRBs (HMXRBs), 13	Swift, XMM-Newton, eROSITA, NICER
Ultraluminous X-ray sources (ULXs), 4		Swift, Chandra, XMM-Newton, ROSAT

Notes. N indicates the number of included objects. We also list the observatories that were used in the creation of the light curves (including upper limits). Observatories used include Swift (Burrows et al. 2005), BeppoSAX (Boella et al. 1997), Chandra (Weisskopf et al. 2000), the X-ray Multi-Mirror Mission (XMM-Newton; Jansen et al. 2001), the Advanced Satellite for Cosmology and Astrophysics (ASCA; Tanaka et al. 1994), the Roentgen Satellite (ROSAT; Trümper 1990), the Spectrum-Roentgen-Gamma (SRG) extended Roentgen Survey with an Imaging Telescope Array (eROSITA; Predehl et al. 2021), the Rossi X-ray Timing Explorer (RXTE; Jahoda et al. 1996), the Monitor of All-Sky X-ray Image (MAXI; Matsuoka et al. 2009), the Hard X-ray Modulation Telescope (Insight-HXMT; Zhang et al. 2020), and the Neutron Star Interior Composition Explorer (NICER; Arzoumanian et al. 2014).

^a We represent the six *candidate* stellar surface SBOs, which overlap entirely with the population of subluminous GRBs, in parentheses for completeness.

(Nakar & Sari 2010). SBOs are short duration when their emission peaks in the X-rays, and there is only one broadly accepted observation (Soderberg et al. 2008; see, however, Mazzali et al. 2008 for a different interpretation), which was a serendipitous detection from a normal Type Ib SN, SN 2008D. While searches of archival data yield potential SBO candidates (e.g., Alp & Larsson 2020; Novara et al. 2020), wide-field X-ray instruments are vital for growing the sample of SBO observations. We note that later analysis of the prompt X-ray signal at the location of SN 2008D showed what is thought to be a breakout from the stellar wind (Balberg & Loeb 2011; Svirski & Nakar 2014). We tentatively include subluminous GRBs as candidate stellar surface breakouts associated with energetic Type Ic-BL SNe in Figure 3. Subluminous GRBs are considered candidate stellar surface breakouts by Nakar (2012), and this possibility is also addressed by Campana et al. (2006), Nakar (2015), and Irwin et al. (2021).

EXMM 023135.0–603743 (Alp & Larsson 2020; Novara et al. 2020), on the other hand, is not included as a candidate in the DLPS owing to the uncertain nature of its progenitor. In addition to the possibility that it is an SBO from a core-collapse SN, both Alp & Larsson (2020) and Novara et al. (2020)

discuss alternative physical scenarios that could give rise to the observed X-ray transient.

In order to better populate the X-ray phase space (Figure 3), we supplement the proposed stellar surface SBO light curves (from subluminous GRBs) with results from theoretical calculations by Nakar (2012). These authors show that

$$E_{\text{bo}} \approx 6 \times 10^{46} E_{53}^{2.3} M_{\text{ej},5}^{-1.65} R_5^{0.7} \text{ erg} \quad (1)$$

$$T_{\text{bo}} \approx 700 E_{53}^{1.7} M_{\text{ej},5}^{-1.2} R_5^{-0.95} \text{ keV} \quad (2)$$

$$t_{\text{bo}}^{\text{obs}} \approx 0.06 E_{53}^{-3.4} M_{\text{ej},5}^{2.5} R_5^{2.9} \text{ s} \quad (3)$$

$$L_{\text{bo}} \approx 4 \times 10^{47} E_{53}^{5.1} M_{\text{ej},5}^{-3.65} R_5^{-1.85} \text{ erg s}^{-1}, \quad (4)$$

where E_{bo} , T_{bo} , $t_{\text{bo}}^{\text{obs}}$, and L_{bo} refer to the breakout energy, temperature, observed time (duration), and luminosity, respectively. E_{53} is energy in terms of 10^{53} erg, $M_{\text{ej},5}$ is the ejecta mass in terms of $5 M_{\odot}$, and R_5 is the stellar radius in terms of $5 R_{\odot}$.

We use a grid of energy values (between 10^{51} and 10^{52} erg), ejecta mass (between 1 and $10 M_{\odot}$), and stellar radius (10^{10} and 10^{11} cm, which span the properties of Wolf-Rayet-like stars) to compute E_{bo} , T_{bo} , t_{bo} , and L_{bo} from Equations (1)–(4). Though a red supergiant with a breakout energy of 10^{52} erg is a

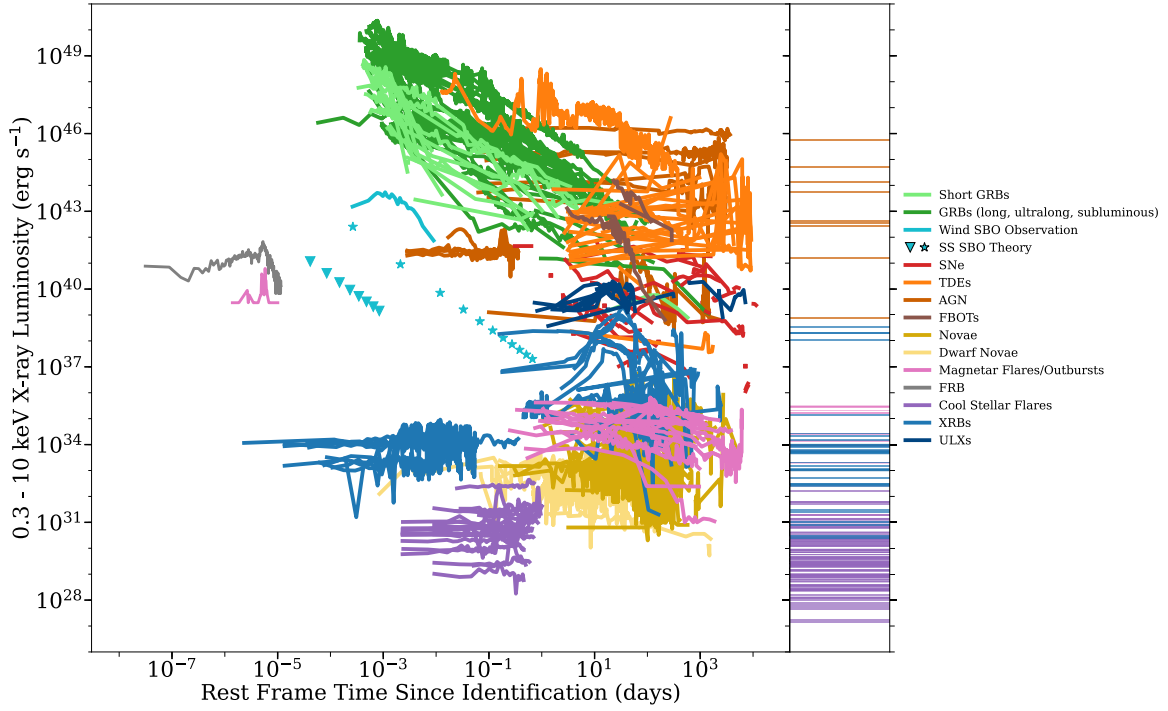


Figure 1. X-ray phase space of transients and variable phenomena, including GRB afterglows, SNe, SN SBOs, TDEs and AGNs, FBOTs, CVs, magnetar flares/outbursts and FRBs, cool stellar flares, XRB outbursts, and ULXs. Main panel: X-ray luminosity evolution with rest-frame time since identification. Theoretical SBO peak L_X -duration points are shown with different symbols corresponding to the model's input parameters; see Section 2.2 for details. Right side panel: to offer a sense of their persistent behavior, the quiescent/preflare luminosities of the included variable classes (AGNs, magnetar flares/outbursts, cool stellar flares, XRBs, and ULXs) are shown as horizontal bars.

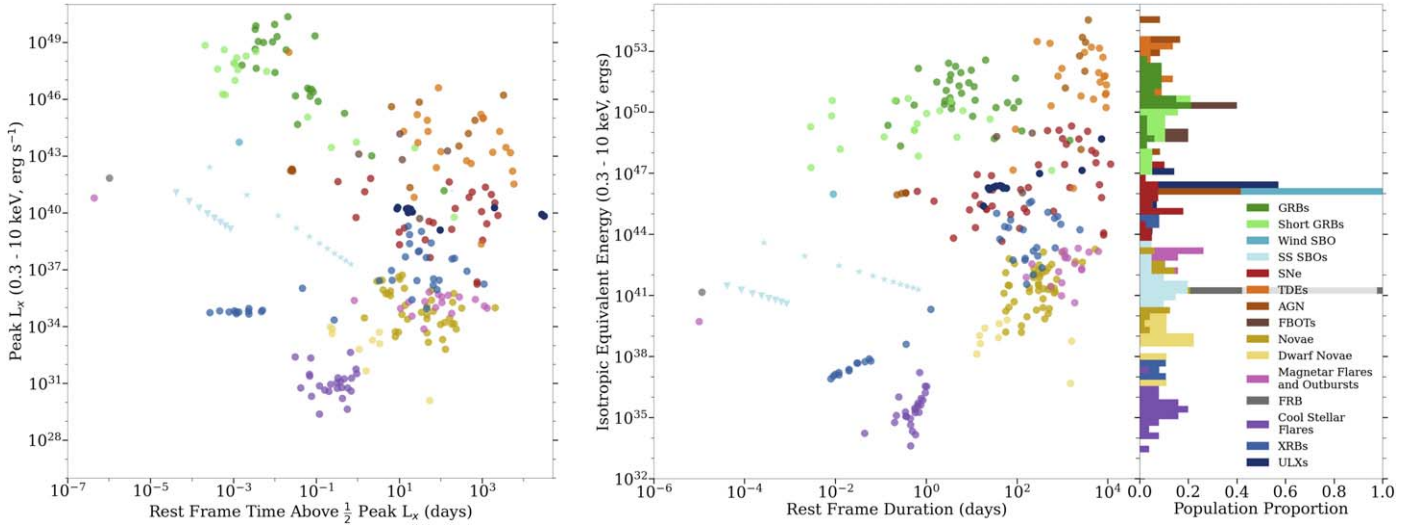


Figure 2. Left panel: the peak X-ray luminosity vs. time above half-maximum light. Right panel: at left, the overall energy released during the event vs. the duration of the transient event, and at right, the distribution of isotropic equivalent energies released for each class of transient/variable. As in Figure 1, theoretical SBO peak L_X -duration point markers correspond to different input parameters in the model. Points are colored according to the class of transient to which they belong; we use the same color coding as in Figure 1 and the histogram at the far right.

less likely physical scenario, we include it anyway to account for the full range of possible progenitors that give rise to SBOs within the phase space. Similarly, in order to populate the phase space with potential durations versus peak luminosities, we limit our plotted sample to those with temperatures (from Equation (2)) in the range 0.1–20 keV as representative of the SBOs that will have some X-ray luminosity component in the 0.3–10 keV range of interest. In the top right panel of Figure 3, each individual point represents the peak luminosity and duration of a single theoretical stellar surface SBO event.

SBOs from the stellar wind like in SN 2008D evolve on timescales ranging from seconds to minutes with $L_X \sim 10^{42}$ – 10^{44} erg s $^{-1}$, making it challenging to observe them without wide-field X-ray instruments facilitating serendipitous detection. Candidate stellar surface SBOs (as potentially in subluminal GRBs) range in luminosity from $\sim 10^{41}$ to 10^{47} erg s $^{-1}$, varying on timescales of $\sim 10^{-4}$ to 10^{-1} days. Our modeled stellar surface SBOs (Nakar 2012) are somewhat less luminous and shorter-lived, with $L_X \sim \text{few} \times 10^{36}$ erg s $^{-1}$ to 10^{43} erg s $^{-1}$ and $t \sim \text{several} \times 10^{-5}$ days to ~ 1 day.

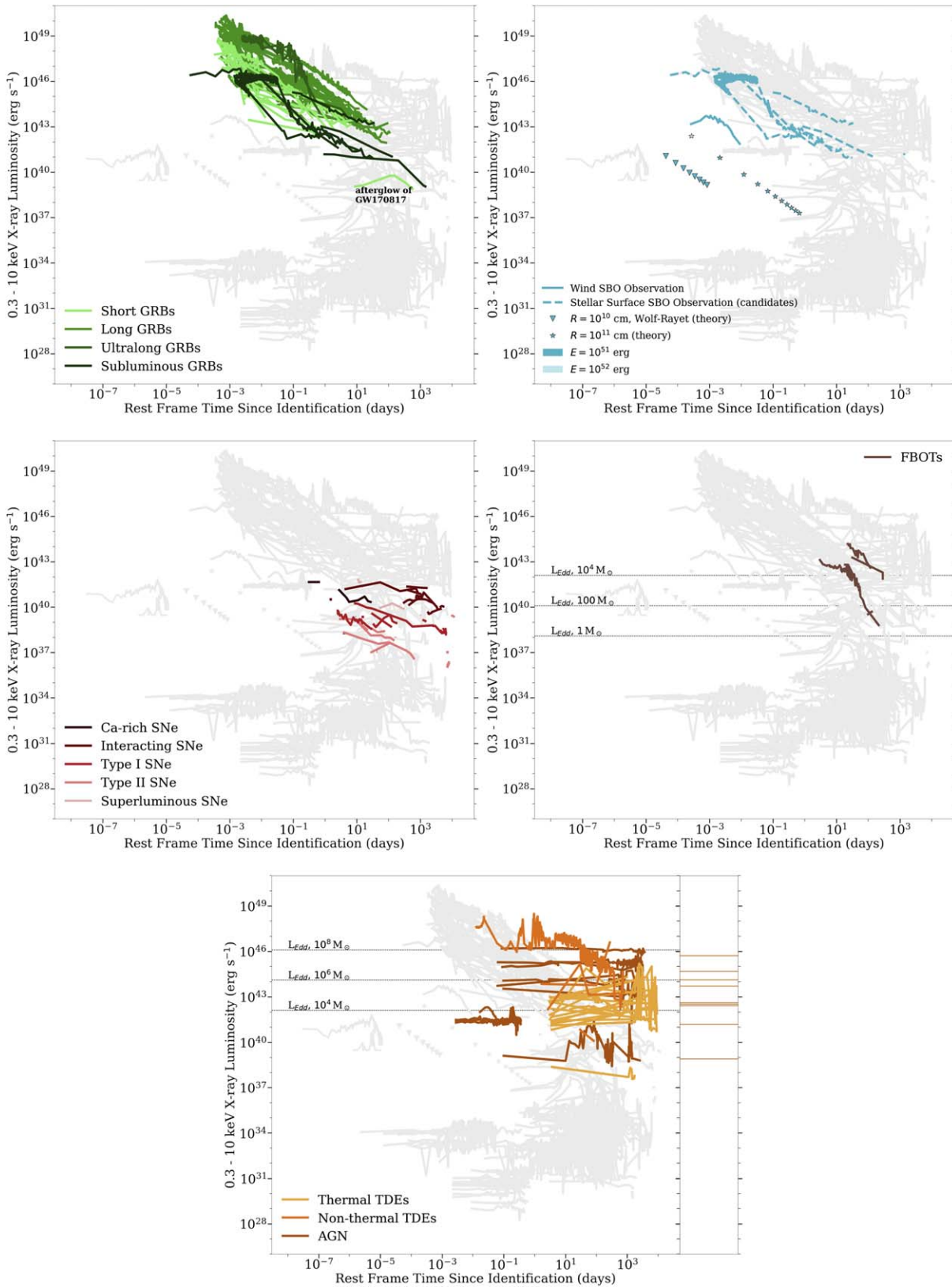


Figure 3. X-ray phase space of extragalactic transients, including GRBs, SBOs, SNe, TDEs, AGNs, and FBOTs, with all other classes of transients from this work underplotted in gray. Peak luminosity vs. duration is shown as points for modeled SBOs (Nakar 2012), with input progenitor radius and breakout energy indicated in the legend by R and E , respectively. We underplot Eddington luminosities (as horizontal dashed lines) for some potentially relevant BH progenitor masses for both FBOTs and TDEs/AGNs (Ramsden et al. 2022; Yao et al. 2023). The FBOT X-ray counterparts occupy a luminosity range that is intermediate between normal SNe (shades of red) and GRBs (shades of green). At right in the TDE/AGN panel, we show preflare AGN luminosities for all included AGNs. Included events are listed in Tables A1–A5.

2.3. Supernovae

SN (Table A3) shocks that propagate in the explosion’s environment are well-known particle accelerators and well-known sources of X-ray emission as the shocks decelerate and the particles cool down (e.g., Chevalier & Fransson 2017 for a recent review). We collected X-ray data for SNe from a variety of sources (see Appendix A for details). Because of the rather limited sample of existing observations, we include all available ($z \leq 1$) X-ray light curves in bands with lower energy limits between 0.2 and 0.5 keV and upper energy limits between 8 and 12 keV, which are then k -corrected to the observed 0.3–10 keV energy band assuming a spectrum $F_\nu \propto \nu^{-\beta}$ with a spectral index $\beta = 1$ (equivalent to a photon index $\Gamma = 2$), which is consistent with observed spectral properties of SNe in the X-rays (e.g., Li & Pun 2011). Even at the most extreme ends of our allowed input energy limits, using $\Gamma = 1$ or $\Gamma = 3$ instead represents a difference of less than a factor of two in luminosity. These k -corrected data are shown in Figure 3.

We divide the SNe into three subclasses based on their underlying physical properties: *Type I core-collapse*, to be composed of Type Ib, Ic, Ib/c, Ic/pec, and Iib SNe; *Type II core-collapse*, to be composed of Type II, IIP, IIL, and Ipec SNe; and *Interacting SNe* (i.e., SNe with signatures of CSM interaction in their optical spectra), to be composed of Type IIn, Ibn, and Ia-CSM SNe. Additionally, we designate (optically) *superluminous SNe* (SLSNe) and *Ca-rich SNe* separately as the two subclasses of SNe for which X-ray emission has been most recently found.

Unlike GRBs, SNe are generally not monitored in the X-rays, in part because they are intrinsically much fainter in the X-rays than GRBs. As a result, they have relatively sparse observations. We include what (non-upper-limit) detections are available in the DLPS. We are complete with respect to published X-ray light curves of SNe through the end of 2012, and we have tried to be complete for all nonordinary SNe (Ca-rich, superluminous, Ia-CSM) with X-ray detections by the time of submission.

Within the DLPS, SNe evolve on timescales ranging from 10^{-1} to 10^4 days. Ca-rich and interacting SNe have luminosities $\sim 10^{39}$ – 10^{42} erg s $^{-1}$ with Ca-rich SNe evolving on timescales between 0.1 and \sim hundreds of days and interacting SNe evolving on timescales between 1 and thousands of days. In general, optically superluminous SNe are less luminous in the soft X-rays with typical $L_X \sim$ several $\times 10^{40}$ erg s $^{-1}$ to several $\times 10^{41}$ erg s $^{-1}$. Type I core-collapse SNe are slightly less luminous with $L_X \sim 10^{38}$ – 10^{40} erg s $^{-1}$, and Type II core-collapse SNe are the least luminous with most light curves spanning $L_X \sim$ several $\times 10^{35}$ erg s $^{-1}$ to 10^{39} erg s $^{-1}$. Further discussion of the differences in the observed X-ray light curves of different classes of SNe can be found in Dwarkadas & Gruszko (2012; see Bietenholz et al. 2021 for a similar discussion in the radio).

2.4. Tidal Disruption Events and Active Galactic Nuclei

TDEs (Table A4) occur when a star passes close enough to a black hole that stellar material is accreted, resulting in high-energy electromagnetic emission from that accretion (Carter & Lummett 1982, 1983).

We include TDEs with both thermal X-ray emission and nonthermal X-ray emission in Figure 3, using Komossa (2015)

and Auchettl et al. (2017) to inform our selection of ($z \leq 1$) TDE candidates, showing only X-ray TDEs and “Likely X-ray TDEs” from the latter. Our sample of TDEs is complete (and robust for merging multiple catalogs) until 2017.

TDEs with nonthermal X-ray emission (hereafter nonthermal TDEs) belong to a subset of $\sim 10\%$ of the TDE population that showed evidence for highly collimated ejecta in the form of relativistic jets (Alexander et al. 2020). There is no evidence for collimation of the thermal X-ray emission, which implies that TDEs with thermal X-rays (hereafter thermal TDEs) are easier to detect. Because there might be similarities between the flare mechanisms of TDEs and AGNs and the distinction between the two classes can be observationally challenging, we opt to show them both in the bottom panel of Figure 3. In the interest of examining only flaring/outbursting behavior, we include long-term variability from AGNs, while we exclude changing-look AGNs, which exhibit more persistent variability. We convert the sample of light curves (Auchettl et al. 2018) to our 0.3–10 keV energy band, assuming $\Gamma = 1.8$ (Tozzi et al. 2006). We note that, though we are far from showing *all* AGN light curves in this energy band, we aim to show a representative sample that demonstrates the difficulty in separating TDEs and AGNs from light curves alone (for additional AGN/blazar light curves, see, e.g., Giommi et al. 2019).

The quasi-periodic eruptions (QPEs) from GSN 069 (Miniutti et al. 2019) occupy a slightly different (similar luminosity, shorter duration) part of the phase space, with $L_X \sim 10^{41}$ – 10^{42} erg s $^{-1}$ and $\sim 10^{-3}$ to 10^{-1} days (AGNs have X-ray luminosities between a few $\times 10^{38}$ erg s $^{-1}$ and $\gtrsim 10^{46}$ erg s $^{-1}$ and vary on timescales of 10^{-1} to 10^3 days; here the low-luminosity end of the range is set by NGC 4395, see Auchettl et al. 2018). The physical mechanism that drives QPEs is not fully understood, so we include an example for consistency in looking at AGN outbursting activity, though they may be associated with the same mechanism as changing-look AGNs.

While the archetypal nonthermal TDE Swift 1644+57 was initially mistaken for a long GRB, Figure 3 shows that TDEs are clearly distinguished from GRBs for their luminous (nonthermal TDEs have luminosities between 10^{42} and 10^{49} erg s $^{-1}$, while thermal TDEs are somewhat less luminous with $L_X \sim 10^{37}$ – 10^{45} erg s $^{-1}$) and *persistent* X-ray emission lasting hundreds of days.

2.5. Fast Blue Optical Transients

FBOTs (Table A5) are a new class of transient astronomical event, only recently recognized in observations and the literature (e.g., Drout et al. 2014; Arcavi et al. 2016; Tanaka et al. 2016; Pursiainen et al. 2018; Ho et al. 2021). In the optical bands, these transients are characterized by short rise times (evolution on the timescale of days) and can reach high luminosities ($L \gtrsim 10^{44}$ erg s $^{-1}$). We include the five known (as of 2022 October) X-ray instances of this class—CSS 161010 (Coppejans et al. 2020), AT 2018cow (Rivera Sandoval et al. 2018, 2019; Margutti et al. 2019), AT 2020xnd (Bright et al. 2022; Ho et al. 2022), AT 2020mrf (Yao et al. 2022), and AT 2022tsd (Matthews et al. 2022; Schulze et al. 2022)—in our phase-space plot, Figure 3. Until now, only the most luminous optical FBOTs (collectively referred to as Luminous FBOTs—LFBOTs) have exhibited detectable X-ray counterparts.

2.6. Cataclysmic Variables

CVs (Table A6) are binary systems undergoing mass transfer in which a white dwarf accretes material from a low-mass main-sequence companion. The conditions of that mass transfer define the characteristics of the CV outburst. Here we look exclusively at the two classes of CVs that exhibit bursting behavior²³—(classical and recurrent) novae and dwarf novae.

A classical/recurrent nova outburst occurs when the accreted material causes thermonuclear runaway on the surface of the white dwarf, resulting in highly energetic ejection of material from the stellar surface. All X-ray data of these novae are from Mukai et al. (2008) and Page et al. (2020); we include all classical/recurrent novae detected between 2006 and 2017. In the instances where we have both an upper- and lower-limit luminosity for various novae in Mukai et al. (2008), we utilized both, to return a *lower-* and *upper-*limit light curve, offering us a greater sense of where novae can, and do, exist in the X-ray phase space (Figure 4). Where *k*-corrections are necessary to shift data into the (observer-frame) 0.3–10 keV energy band, we adopt a thermal bremsstrahlung spectral model with $kT = 5$ keV following Mukai et al. (2008).

The X-ray emission in dwarf novae stems from the inner accretion flow region around the white dwarf. During the outburst, the mass transfer rate through this inner region increases. As a result, it is expected that the X-ray emission (≥ 2 keV) will briefly increase but then be suppressed as the optical depth of this region increases. This behavior can be seen in multiwavelength light curves of the dwarf nova SS Cygni (e.g., Wheatley et al. 2003; Russell et al. 2016). Note that there are a number of unanswered questions about this model (see Mukai 2017), and no other dwarf novae show this exact behavior (e.g., Fertig et al. 2011; Mukai 2017). As we are interested in the DLPS of systems that show X-ray brightenings, we limit our sample to those dwarf novae that show X-ray brightenings during optical outburst (see Table A6). The three dwarf novae included here are those with good temporal coverage and multiwavelength data that support enhancement in the X-rays. There are ~ 8 other dwarf novae that show this same brightening, but each has only ~ 1 detection in outburst.

CV outbursts are fairly low luminosity in the $L_X \sim 10^{28}$ – 10^{36} erg s⁻¹ range, with dwarf novae only reaching a peak $L_X \sim 10^{34}$ erg s⁻¹ and classical/recurrent novae spanning that entire range. They evolve on timescales ranging from seconds to years.

2.7. Magnetar Flares/Outbursts and Fast Radio Bursts

Magnetar flares/outbursts (Table A7), driven by perturbations in the strong magnetic field of the magnetar, come in three broad flavors: giant flares (to date, only observed in the hard X-rays and gamma-rays), outbursts (characterized by a decay on the scale of days), and intermediate flares/short bursts (lasting milliseconds to tens of seconds). At gamma-ray energies, the three observed giant flares started with a short (0.1–0.2 s) flash with luminosity from $\approx 10^{44}$ to 10^{46} erg s⁻¹, which was followed by a tail lasting a few hundreds of seconds and modulated at the pulsar spin period. In all three events, the total energy of the tail was $\approx 10^{44}$ erg (e.g., Esposito et al. 2021). While it is likely that a comparable amount of energy

was emitted in the soft X-ray band (see Rea et al. 2013), we lack reliable measurements of their properties in that band.

Though intermediate flares and short bursts are often referred to separately, Israel et al. (2008) suggest that these events actually occur along a continuum of spectral properties (though not a continuum in duration or fluence). Making an arbitrary cut, where intermediate flares persist longer and are brighter while short bursts are lower energy and shorter duration, is not based on intrinsically different physics. For the purposes of simplicity in our subclassifications, we consider intermediate flares and short bursts to be a single population, characterized by $L_X \sim 10^{39}$ – 10^{41} erg s⁻¹ and varying on extremely short timescales $\sim 10^{-6}$ to 10^{-4} days.

We used the Magnetar Outburst Online Catalog (Coti Zelati et al. 2018) for most of the *outburst* data ($L_X \sim 10^{31}$ – 10^{46} erg s⁻¹ with variation on timescales $\sim 10^{-1}$ – 10^4 days), also including data from Rea et al. (2016) and Esposito et al. (2019) in order to build a *representative* sample. Plotting each light curve from the beginning of the outburst itself, we show each recurrent event from the same progenitor separately.

In order to elucidate the variable nature of these magnetars, we compare their luminosity in outburst (or during a flare) to their quiescent luminosity; we retrieve these data from Olausen & Kaspi (2014)²⁴ in the 2–10 keV energy band. We employ a *k*-correction, to appropriately relate these luminosities to the 0.3–10 keV behavior we have emphasized throughout the X-ray phase-space plot, given a power-law, blackbody, or power-law + blackbody model individual to the source from Olausen & Kaspi (2014). Where a spectral fit is not offered, we use a generalized multiple component spectrum ($\Gamma \sim 2$, $kT_{\text{low}} \sim 0.3$ keV, $kT_{\text{high}} \sim 0.6$ keV) in quiescence (Mong & Ng 2018). Further, to ensure a one-to-one comparison of the emission from quiescent magnetars and those actively exhibiting variable behavior, we restrict our quiescent L_X sample to match the magnetars shown in the X-ray phase space plot (Figure 4).

Due to the extremely fleeting nature of the short bursts and intermediate flares, many of the data come from serendipitous triggers, many of which occur in the harder X-rays, since the current class of wide-field instruments operate in the hard X-rays/gamma-rays. This accounts, in part (or in whole), for the paucity of observations for these phenomena in the soft X-rays (and so in our phase-space plot) relative to the frequency with which they occur.

FRBs are extremely short duration transient events characterized by an intense burst of radio emission (Lorimer et al. 2007; or see Petroff et al. 2019, 2022 for reviews). Multi-wavelength follow-up has been conducted to detect counterparts in other wavelength regimes, but efforts have been largely unsuccessful (e.g., Chen et al. 2020). Recently, though, the SGR 1935+2154 outburst on 2020 April 28 has been the subject of discussion as a candidate for an X-ray counterpart to FRB 200428 (Bochenek et al. 2020; The CHIME/FRB Collaboration et al. 2020). Concurrent radio and X-ray emission from this source was detected again in 2022 October (Dong & CHIME/FRB Collaboration 2022; Wang et al. 2022).

Because there is evidence linking this event to a magnetar progenitor, we include the FRB light curve (Li et al. 2021) in Figure 4. The coincident X-ray event from SGR 1935+2154 is consistent with the apparent continuum behavior of magnetar

²³ We do not include light curves from nonoutbursting CVs, like polars, which exhibit low-amplitude flickering and flaring due to their stronger magnetic fields (e.g., Angelini & Verbunt 1989).

²⁴ <http://www.physics.mcgill.ca/~pulsar/magnetar/main.html>

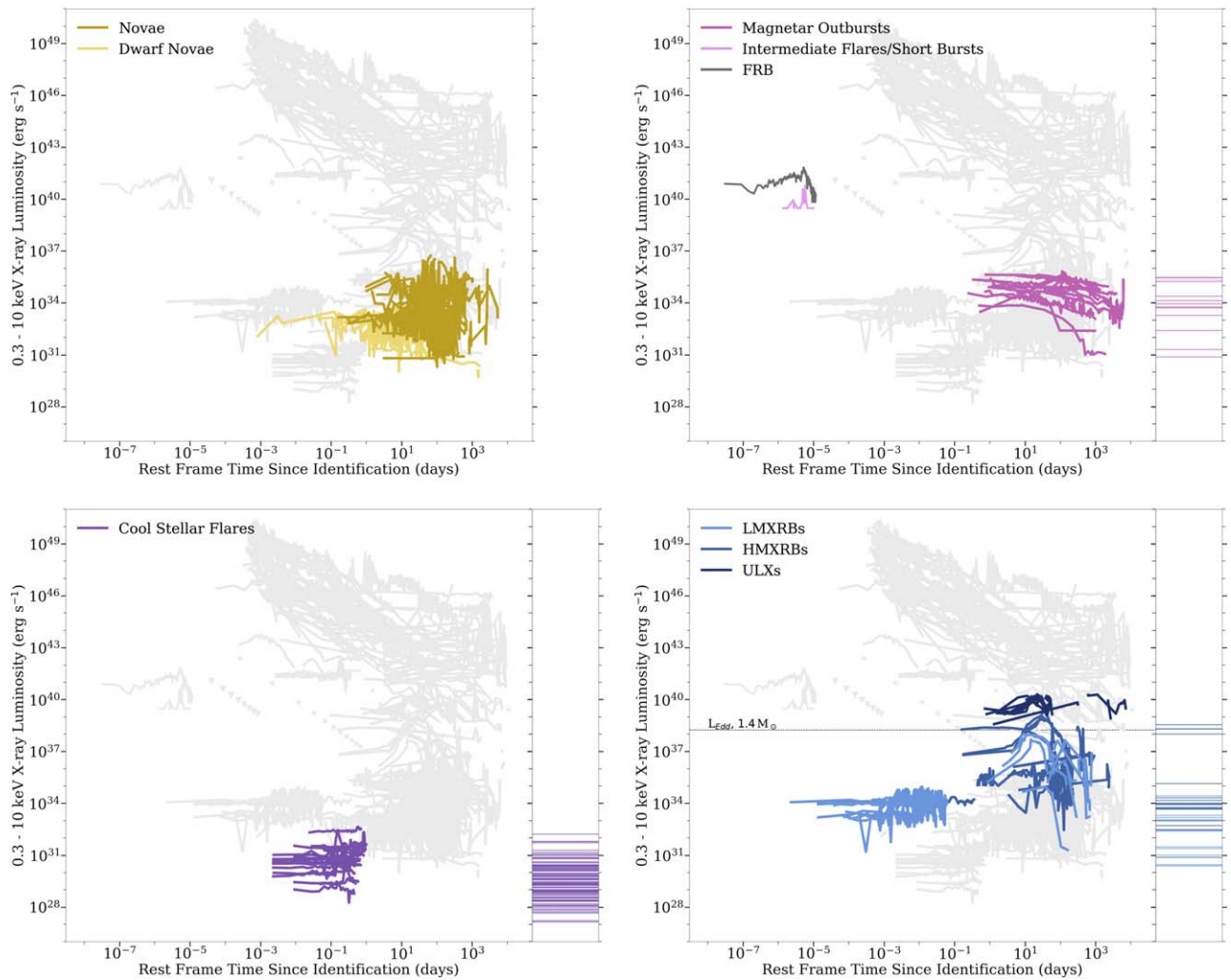


Figure 4. X-ray phase space of Galactic (CVs, magnetar flares/outbursts, and cool stellar flares) and Galactic/extragalactic (XRBs, ULXs, and FRBs) transients and variables, including those classes of event with some signals that have been observed to originate within the Galaxy, such as CVs (novae and dwarf novae), magnetar flares and outbursts, FRBs (specifically the Galactic FRB 200428), cool stellar flares, XRBs, and ULXs. We underplot the Eddington luminosity for a $1.4 M_{\odot}$ progenitor for additional context in the XRBs/ULX panel. With the exception of the CV panel, at right, we show quiescent luminosities for each class of object. Included events are listed in Tables A6–A9.

outbursts, flares, and bursts across the phase space (with $L_X \sim 10^{40} - 10^{42} \text{ erg s}^{-1}$ on timescales $\sim 10^{-8}$ to 10^{-5} days) and is indicative of the possibility that some FRBs might be the radio counterparts to soft gamma repeaters (see, however, Pleunis et al. 2021).

2.8. Cool Stellar Flares

Cool, low-mass stars (Table A8), such as M dwarfs, can be highly variable, with energetic flares driven by magnetic reconnection events. The intensity of this behavior is also correlated with age, with younger low-mass stars exhibiting more variability.

We place data from Pye et al. (2015) in Figure 4 and assume a thermal spectral model with a temperature of $kT = 1.5 \text{ keV}$ in order to perform the flux conversion. Dwarf stars included in our sample are K, M, and L types. As in Section 2.7, quiescent luminosities (digitized from Pye et al. 2015) are plotted at the right to appropriately contextualize the flares and offer yet more indication of where these flaring stars exist in the X-ray phase space. Cool stellar flares are relatively short duration, with timescales ranging from on the order of hundreds of

seconds up to ~ 1 day. They are also low-luminosity²⁵ events with $L_X \gtrsim 10^{28} \text{ erg s}^{-1}$ and up to several $\times 10^{32} \text{ erg s}^{-1}$. Quiescent luminosities span the range $\sim 10^{27} - 10^{32} \text{ erg s}^{-1}$.

2.9. X-Ray Binary Outbursts and Ultraluminous X-Ray Sources

XRBs (Table A9) are stellar binaries where a compact object (neutron star or black hole) is accreting material from its companion, causing energetic outbursts. ULXs (characterized by peak $L_X > 10^{39} \text{ erg s}^{-1}$, independent of the source’s underlying mechanism) are frequently associated with super-Eddington XRBs. We also elect to group them here, showing them in the same panel of Figure 4. XRBs are further broken out into high-mass (HMXRBs, with a companion star of mass $\gtrsim 10 M_{\odot}$; for a review, see Reig 2011) and low-mass (LMXRBs, generally with an $M \lesssim 1.5 M_{\odot}$ companion; for a review, see Tetarenko et al. 2016) populations. The former includes Be XRBs, supergiant XRBs, and supergiant fast X-ray transients, while the latter includes neutron star XRBs, black

²⁵ We note that all-sky survey data have shown intrinsically rare flares up to $L_X \sim 10^{34} \text{ erg s}^{-1}$ at slightly higher energies (2–20 keV; Tsuboi et al. 2016).

hole XRBs, and, though we do not have any in our DLPS sample, very faint X-ray transients (Heinke et al. 2015) or very faint XRBs. Details of the relevant data and their provenance are given in Table A9.

As with the other variable signals (magnetar outbursts and cool stellar flares; top right and bottom left panels of Figure 4), we plot the quiescent L_X of ULX and XRB events at the right in Figure 4. As in Section 2.7, for the purposes of this paper, we define the quiescent luminosity as the lowest recorded X-ray luminosity, opting for simplicity rather than a more stringent definition that might not designate this persistent, nonoutburst behavior as quiescence. Though we are not aiming for completeness, choosing instead to use a *representative* sample, the XRB and ULX coverage of the phase space is clear for relatively long timescales ranging from tenths to thousands of days and intermediate luminosities. XRBs exist in roughly the $L_X \sim 10^{32} - 10^{39} \text{ erg s}^{-1}$ range (with quiescent luminosities between 10^{30} and $10^{35} \text{ erg s}^{-1}$ and outburst $L_X \gtrsim 10^{35} \text{ erg s}^{-1}$). ULXs have luminosities greater than several $\times 10^{38} \text{ erg s}^{-1}$ and up to $\sim 10^{40} \text{ erg s}^{-1}$, with quiescent L_X falling between 10^{38} and $10^{39} \text{ erg s}^{-1}$.

With regard to target selection, it is necessary to use a sample of sources with well-measured distances. We note that many of the Galactic HMXRBs have poorly measured distances with high uncertainties (e.g., Bartlett et al. 2019; Ferrigno et al. 2022), while their soft X-ray spectra might suffer from strong absorption. However, nearby galaxies of the Small and Large Magellanic Clouds (i.e., SMC and LMC) have well-defined distances, low foreground absorption, and an abundance of HMXRBs (Haberl & Sturm 2016). Thus, a representative sample of HMXRB outbursts was obtained from the SMC and LMC.

3. Discussion

3.1. Unclassified X-Ray Sources: A Short Case Study

With the rise of time-domain astronomy, there has been a commensurate increase in opportunities to capture new types of transient/variable events that defy all known classification schemes. In some cases, these events have been discovered in archival data searches, thus preventing real-time follow-up of these events outside the X-rays. This has practically prevented the identification of the true underlying nature of these new classes of events. In Figure 5, we plot a selection of these yet-identified “oddballs” (Jonker et al. 2013; Glennie et al. 2015; Irwin et al. 2016; Bauer et al. 2017; Xue et al. 2019; Novara et al. 2020) to illustrate how they fit into the larger X-ray phase space. We include only those with known or estimated distances (assuming for the purposes of this case study that the X-ray phase space of transients for $z \leq 1$ is similar to the phase space of transients at all redshifts) and spectra for those observed outside of the 0.3–10 keV energy band to facilitate a k -correction.

Where multiple distance estimates are given, we include light curves at each of those distances to better fill out the *uncategorized* X-ray phase space and demonstrate the potentially varied interpretations of these signals at different redshifts. Though they are sometimes referred to as fast X-ray transients (see, e.g., Quirola-Vásquez et al. 2022, 2023 for a population-level examination), the light curves point to these transients having a variety of progenitors. This inhomogeneous class of transient events evolves on timescales

of roughly tens of seconds to days and spans roughly 21 dex in luminosity.

Where the discovery papers have broadly speculated about the origin of these transients, we have colored the “oddball” light curves accordingly, allowing their position in the DLPS to discriminate between equally likely physical scenarios. In fact, this is an extension of the analysis done in Bauer et al. (2017), where they illustrate potential classifications by comparing CDF-S XT1 to light curves from already-classified events. Where no one potential class is favored in the discovery paper, we choose to leave the light curve *uncategorized* in the X-ray phase space (CDF-S XT1), whereas we color those with a single (or preferred) proposed origin according to that theory (XRT 000519, XRT 120830, XRT 110103, EXMM 023135.0–603743). Jonker et al. (2013) prefer the (beamed) tidal disruption of a white dwarf by an intermediate-mass black hole for XRT 000519, though our results suggest that an X-ray flash (as would be associated with a GRB) would also be reasonable. Taking XRT 000519 as potentially related to XRT 110103, Glennie et al. (2015) suggest the same potential progenitors for that event. They also indicate that XRT 120830 seems consistent with a dwarf star flare, which is borne out by its position in the phase space. Eappachen et al. (2022) examine the potential host galaxies of XRT 000519 and XRT 110103 in order to place constraints on the nature of the fast X-ray transients; though no potential host was detected for XRT 110103, XRT 000519 appears associated in projection with a distant galaxy candidate, seemingly favoring a beamed TDE or a binary neutron star merger like the one responsible for GW170817.

Sources 1 and 2 (Irwin et al. 2016) are ULX outbursts in NGC 4636 and NGC 5128, respectively. Though their behavior is largely consistent with soft gamma repeaters or anomalous X-ray pulsars (their position in the DLPS matches the anticipated position of intermediate-luminosity/duration magnetar flares and outbursts), the stellar populations of their hosts make this scenario unlikely. It is also possible that they are outbursts due to accretion onto neutron stars (though they are super-Eddington in this scenario, these events are somewhat shorter in duration than the other ULXs in the DLPS) or intermediate-mass black holes. In the context of the DLPS, Sources 1 and 2 are also consistent with the anticipated position of smaller, lower-energy stellar surface SBOs. CDF-S XT2 (Xue et al. 2019) has been identified as having emission consistent with a magnetar-driven outburst, potentially from a binary neutron star merger. Its position in the DLPS is strikingly similar to the included population of short GRBs. Xue et al. (2019) rule out long GRBs and SBO-like events owing to the luminosity and luminosity evolution and point out that a beamed TDE is also unlikely owing to the short timescales on which that evolution occurs. Similarly, Novara et al. (2020) posit that EXMM 023135.0–603743 could be an SBO from a core-collapse SN, a possibility that is supported by the light curve’s position in the phase space, while also noting that it could be an AGN (within the DLPS, EXMM 023135 also overlaps almost entirely with the QPE GSN 069), a TDE, or even a late-time observation of a giant flare from a magnetar, though each of those scenarios is disfavored given other concurrent data (Novara et al. 2020).

Ultimately, it is clear that, while the DLPS is not able to provide classification for transients/variables without input from the signal’s spectral evolution and from other

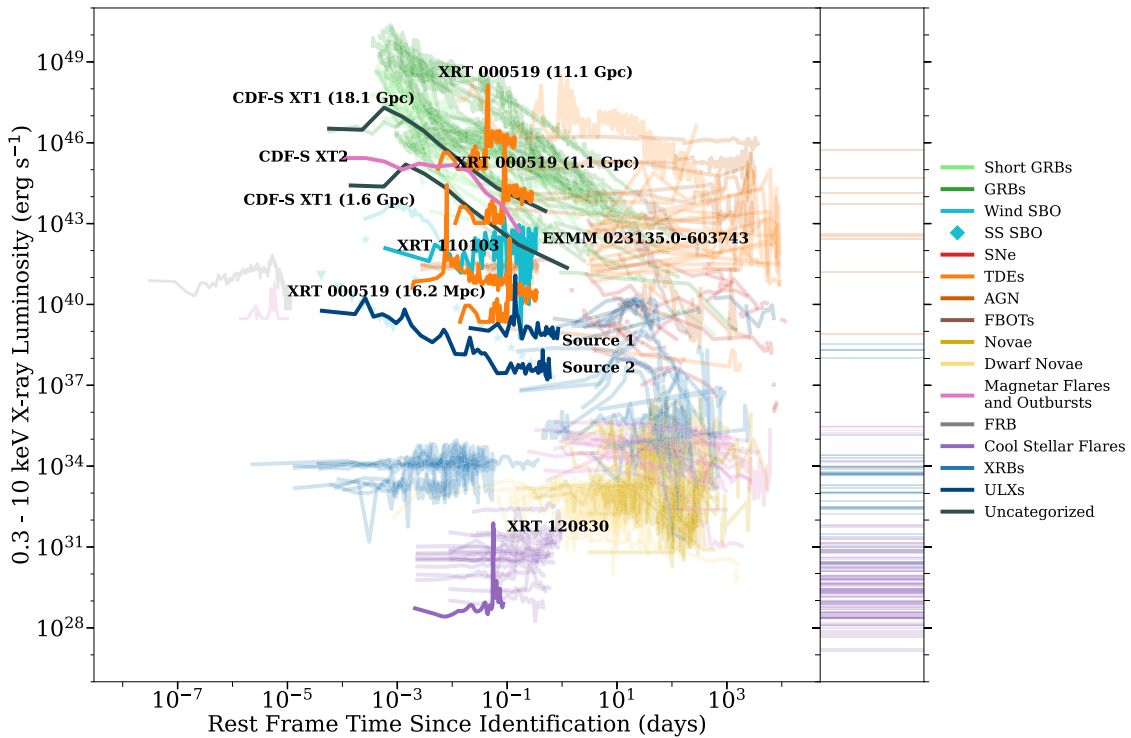


Figure 5. We compare existing observations of transients with unclear/debated classification (Table A10) with our established X-ray phase space as described in Section 3.1. These signals are colored according to their preferred classification, though in cases where no one model is considered a better match (CDF-S XT1), we give them their own “oddball” color to differentiate them from the already classified transients in the phase space. For sources with uncertain distance estimates, each estimate is shown, with the relevant distance stated in parentheses. Included events are listed in Table A10.

investigations that hint at the underlying mechanism, it is extremely useful to contextualize potential and preliminary classifications. As we see looking at the 16.2 Mpc XRT 000519 light curve and XRT 110103, their position in the phase space is apparently more consistent with an AGN/QPE than with a TDE, the potential confusion in classification stemming from the innate difficulty in distinguishing TDEs and AGNs. For greater distances, the light-curve characteristics of XRT 000519 seem to potentially align with a GRB-related X-ray flare. Similarly, while CDF-S XT1 has a myriad of potential progenitors (among them, an off-axis short GRB or a subluminal GRB, another white dwarf–intermediate-mass black hole TDE; Bauer et al. 2017), the light curve (assuming a distance of 18.1 Gpc) is nicely consistent with the subluminal GRBs in our sample.

3.2. Discovery Space

As we enter a new era in the search for/detection of X-ray transients and variables, due to both large time-domain surveys and next-generation X-ray observatories, it is crucial to understand the observational restrictions that have inherently shaped our understanding of the high-energy transient sky to now. In examining the phase space of existing detections, we find that while both the most luminous (largely extragalactic) and least luminous (largely Galactic) part of the phase space is well populated at $t > 0.1$ day, intermediate-luminosity phenomena ($L_X = 10^{34} - 10^{42}$ erg s $^{-1}$) represent a gap in the phase space. We thus identify $L_X = 10^{34} - 10^{42}$ erg s $^{-1}$ and $t = 10^{-4}$ to 0.1 days as a key discovery phase space in transient X-ray astronomy (see Figure 6).

The most obvious constraints are the sensitivity limits of current instruments and the difficulty of rapid response to a

fleeting and intrinsically rare signal, which leave gaps in our phase space at low luminosities and short durations, respectively. Due to inherent design constraints (see Figure 7, discussed more in Section 3.3), current instruments generally fall into one of two categories—instruments that are likely to contribute to the serendipitous discovery of soft X-ray transients, which have limited sensitivity, and instruments that allow for follow-up of event evolution down to very deep limits, which are extremely limited in their FOV.

Instruments with a wide FOV will serendipitously detect many more events than targeted instruments, contributing to the discovery of transient signals alongside survey instruments. Realistically, extremely short duration events (on the order of seconds) will not be observed with any regularity without a new generation of wide-field instruments. This regime of extremely rapid events is already known to include FRB X-ray counterparts and their likely relatives, magnetar flares.

Target-of-opportunity (ToO) protocols and other similar observational triggers play a role in the successful follow-up of transitory signals. Greater efficiency in the form of fast repointings will also help push toward observation of extremely short duration events; for instance, the robust Swift ToO process is well established. Automated follow-up is not restricted to the X-ray, with high-energy transient detections triggering radio observations (e.g., Staley et al. 2013; Hancock et al. 2019), as well.

Projects such as Exploring the X-ray Transient and variable Sky (EXTraS; De Luca et al. 2021) aim to address the gap in the short-duration phase space at the algorithmic level, extracting previously unidentified signals and variability from existing XMM-Newton data (e.g., Novara et al. 2020). Efforts to rapidly disseminate information about detections like the

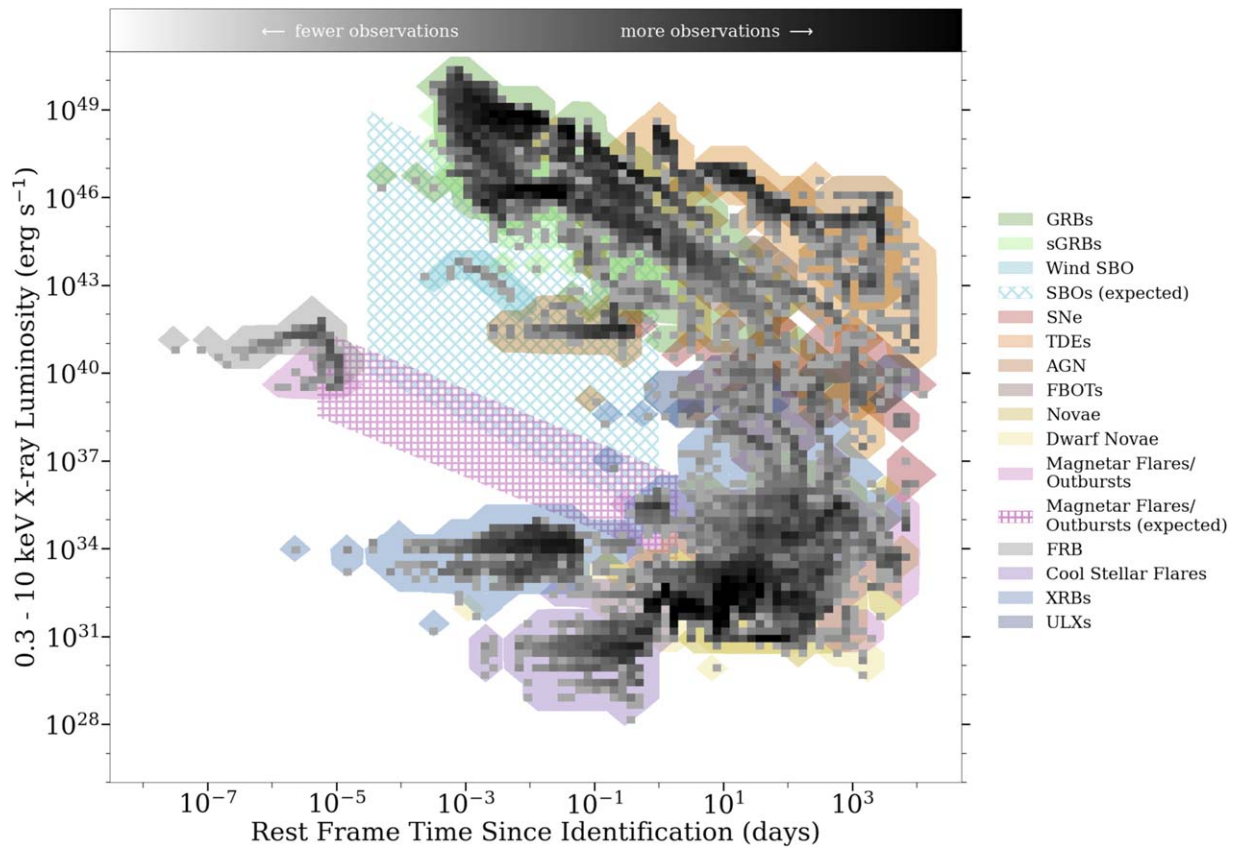


Figure 6. The density of light curves in our phase space with the corresponding classes of transient underplotted; the color bar is logarithmic, and larger bins were used for the transient classes than for the overall observations. Though we only show the density of the representative data included in this paper (and so not the comprehensive density of *all* observations in this energy band, though this sample should span a representative range in observed X-ray luminosity and duration), certain trends are notable that are generally relevant, including that the best-sampled classes of transient are either Galactic phenomena (such as cool stellar flares or novae) or high-luminosity extragalactic transients such as GRBs and short GRBs and that there is a paucity of observations of relatively short duration events at intermediate luminosities. We use crosshatches to mark the general region of the phase space where we would anticipate, but do not yet have, observations of magnetar flares and outbursts (pink) and SBOs from stellar explosions (light blue), among other events. We note that, though it is possible that the soft X-ray emission from giant flares of magnetars may be comparable in luminosity to what has been observed in the hard X-rays (peak $L_X \sim 10^{47}$ erg s^{-1} ; Hurley et al. 2005), given the paucity of soft X-ray observations of giant flares, we define the “expected” region of the DLPS for magnetar flares and outbursts based on available data.

Living Swift-XRT Point Source catalog (Evans et al. 2022) offer yet other opportunities for expedient analysis and follow-up. Similarly, it is possible that mining *unrelated* X-ray observations (e.g., those intended to study the hot halos of galaxies) for transients in real time provides another avenue for serendipitous detection.

More sensitive instruments are key for targeted follow-up. The next generation of highly sensitive soft X-ray missions will enable us to track the evolution of light curves to much later times/lower luminosities as they decay and will provide a broader understanding of transient populations, as in many cases we are currently only meaningfully sampling the most luminous end of the population.

Figure 6 also reveals an undersampled area of the phase space that we should aim to explore. On the interval $L_X = 10^{34} - 10^{42}$ erg s^{-1} and with timescales between 10^{-4} and ~ 0.1 day, there is a clear gap in the phase space. This gap also corresponds to some known physical phenomena—stellar surface SBOs (see Section 2.2) and the continuum behavior between magnetar flares and outbursts (see Section 2.7). Efforts to expand observations in this regime should be motivated by the probable detection of these missing signals.

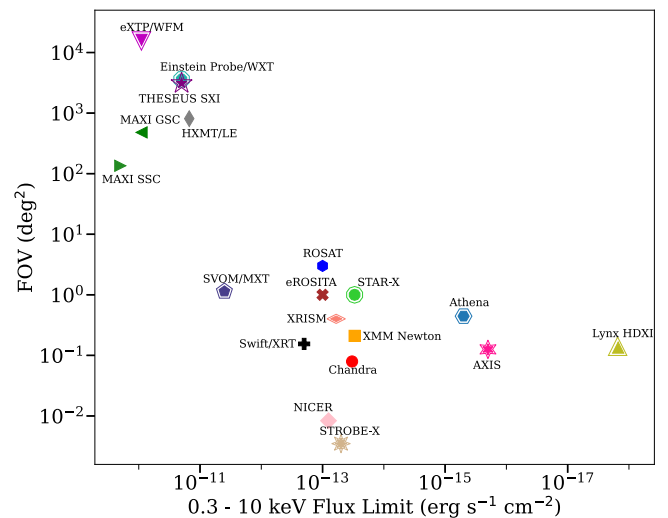


Figure 7. Here we show the roughly inverse relation between instrument FOV and depth with a summary of these specifications for existing and planned/proposed X-ray missions (see Table 2 for more details). We report the 1 ks 0.3–10 keV sensitivity. Upcoming/proposed instruments are highlighted by an additional marker outline.

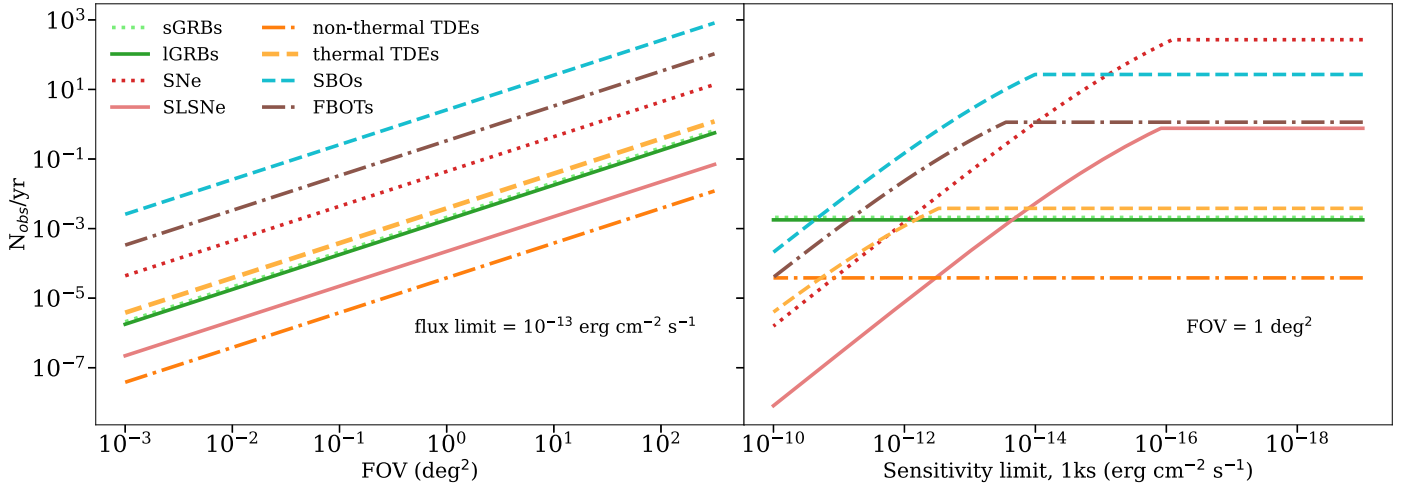


Figure 8. To decouple the advantages of increased FOV and sensitivity, we show extragalactic transient rates (Stone & Metzger 2016; Coppejans et al. 2020; Margutti & Chornock 2021; Ghirlanda & Salvaterra 2022) as a function of FOV with a fixed flux limit (left, sensitivity = 10^{-13} erg s $^{-1}$ cm $^{-2}$) and the same rates as a function of sensitivity with a fixed FOV (right, FOV = 1 deg 2). As in the rest of this work, we limit the rates to $z \lesssim 1$ —which is why the number of observations per year eventually flattens with increasing sensitivity. For luminous sources, like those included here, substantial increases in the number of events detected within $z \lesssim 1$ will primarily come from instruments with increased FOV.

Table 2
Soft X-Ray Imaging Instrument Performance Parameters

Instrument	Energy Band (keV)	Flux Limit ^a (erg s $^{-1}$ cm $^{-2}$)	FOV	References
ROSAT/PSPC-C	0.1–2.5	$\sim 10^{-13}$	3 deg 2	Trümper (1990), Briel et al. (1996) Greiner et al. (1999)
Chandra ACIS-S ^b	0.5–7	$\sim 3 \times 10^{-14}$	16'9 × 16'9	Chandra X-ray Center et al. (2021)
Swift/XRT	0.3–10	$\sim 2 \times 10^{-13}$	23'6 × 23'6	Burrows et al. (2005) Evans et al. (2020)
MAXI GSC	2–30	$\sim 9 \times 10^{-11}$	160° × 3°	Sugizaki (2010)
MAXI SSC	0.5–12	$\sim 2 \times 10^{-10}$	90° × 1'5	Tsunemi et al. (2010)
XMM-Newton/EPIC-pn	0.2–10	$\sim 3 \times 10^{-14}$	27'5 × 27'5	Watson et al. (2001)
SRG/eROSITA	0.2–8	$\sim 10^{-13}$	0.8 deg 2	Merloni et al. (2012)
NICER	0.2–12	$\sim 8 \times 10^{-14}$	30 arcmin 2	Arzoumanian et al. (2014)
Insight-HXMT/LE	0.9–12	$\sim 1.5 \times 10^{-11}$	21 × (1'6 × 6'), 7 × (4° × 6°), 2 × (50° × 60° × 2° × 6°) or ~ 810 deg 2 total	Li et al. (2020b)
SVOM/MXT	0.2–10	$\sim 4 \times 10^{-12}$	64' × 64'	Wei et al. (2016)
XRISM/Xtend ^c	0.4–13	$\sim 6 \times 10^{-14}$	38' × 38'	XRISM Team (2023, private communication)
Athena/WFI	0.2–15	$\sim 5 \times 10^{-16}$	40' × 40'	Barcons et al. (2012)
eXTP/WFM	2–50	$\sim 9 \times 10^{-11}$	$\sim 180^\circ \times 90^\circ$	Zhang et al. (2019)
AXIS	0.1–10	$\sim 2 \times 10^{-16}$	144 π arcmin 2	Mushotzky (2018)
Einstein Probe/WXT	0.5–4	$\sim 2 \times 10^{-11}$	3600 deg 2	Yuan (2017)
STAR-X	0.5–6	$\sim 3 \times 10^{-14}$	1 deg 2	STAR-X Team (2023, private communication)
STROBE-X	0.2–12	$\sim 5 \times 10^{-14}$	4 π arcmin 2	Ray et al. (2019) Meidinger (2018)
Lynx/HDXI	0.2–10	$\sim 1.5 \times 10^{-18}$	22' × 22'	The Lynx Team (2019)
THESEUS/SXI	0.3–5	$\sim 2 \times 10^{-11}$	~ 0.5 sr	Amati et al. (2021)

Notes. We use the horizontal bars to differentiate between four categories of instrument; from top to bottom we list past instruments, currently operational instruments, instruments on future missions selected for launch, and instruments on proposed missions. The list of proposed missions is not complete and is provided to illustrate the range of capabilities of future experiments.

^a 0.3–10 keV; all flux limits are k -corrected to our band of interest assuming a fiducial $\Gamma = 2$ spectrum. Flux limit is based on a 1 ks exposure for instruments that do pointed observations. We note that for instruments designed for higher-energy observations—such as MAXI GSC or eXTP/WFM—our estimated flux limit in the 0.3–10 keV energy band is less secure.

^b The reported Chandra 0.3–10 keV flux limit is estimated from recent observations.

^c We take the full-band Suzaku/XIS flux limit from Miura et al. (2008), given that its sensitivity is roughly comparable to that of XRISM/Xtend (XRISM Team 2023, private communication).

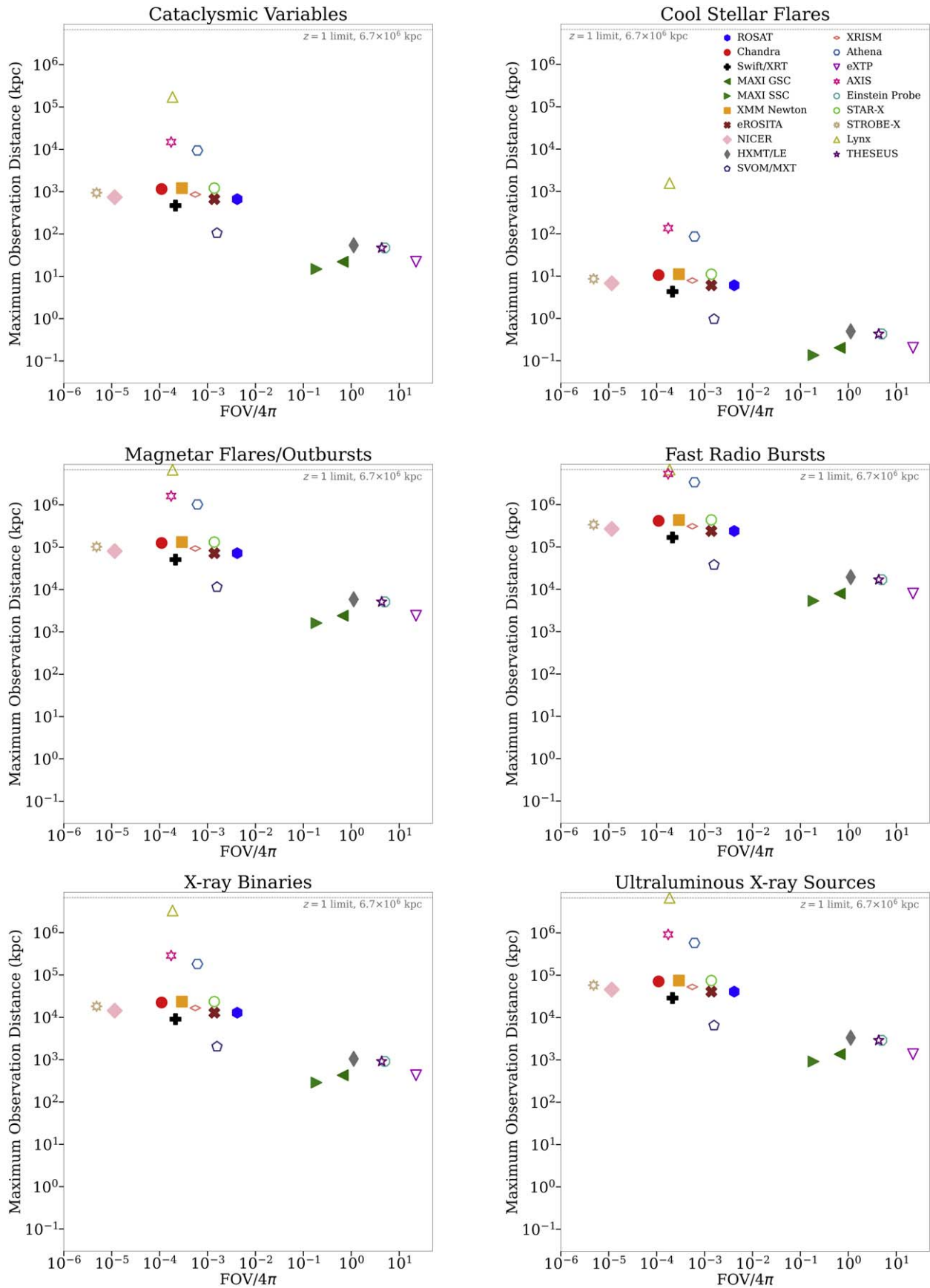


Figure 9. The maximum distance out to which each instrument can observe different classes of transient/variable vs. the normalized FOV (by the area of the sky). As in the rest of this work, we limit to $z \leq 1$ ($d_L = 6.7 \times 10^6$ kpc), which is shown by the gray dashed line. For less luminous classes of transient, the improved sensitivity from proposed/planned instruments (shown with open markers) represents an increase of up to ~ 3 orders of magnitude in the distance out to which these events can be detected and observed. This significantly enlarges the potential observing volume for these signals.

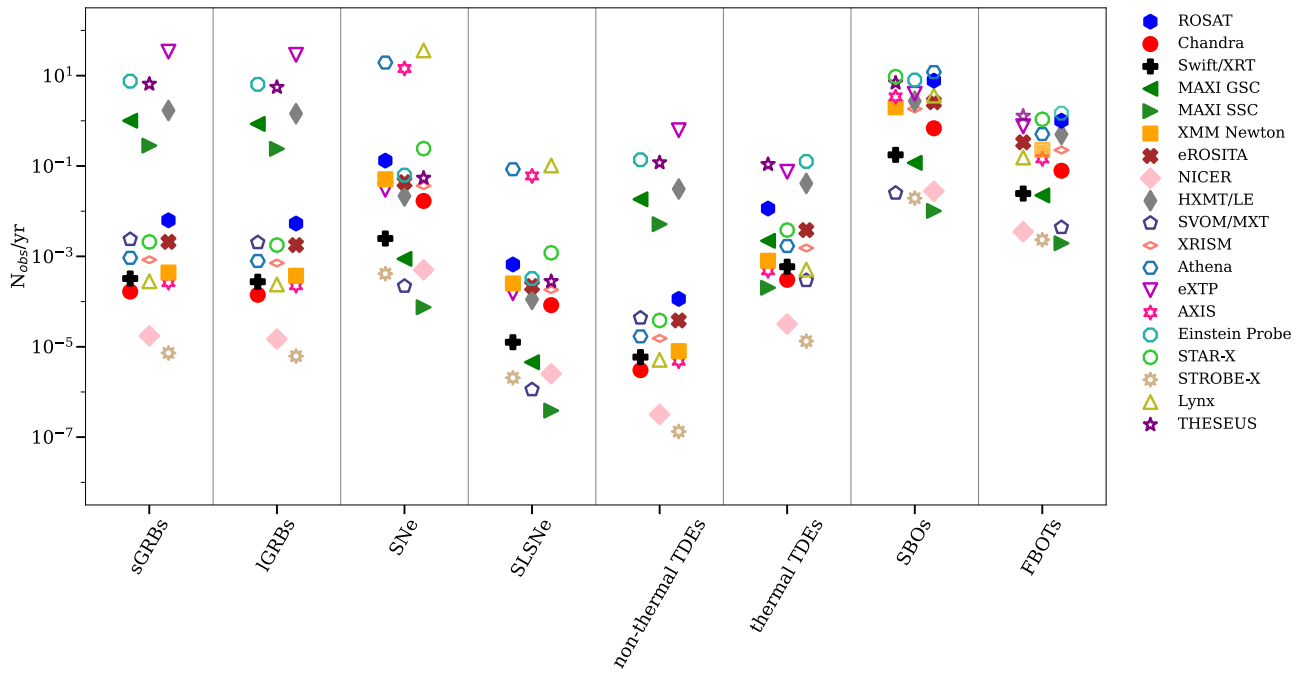


Figure 10. Estimates of the number of serendipitous observations expected per year for transients with a variety of different instruments based on the volumetric rates of the phenomena and the observing volume of each instrument. The comoving depth out to which each instrument can observe each class of phenomenon is calculated based on the peak observed luminosity of each phenomenon, making the assumption that we have already detected the most intrinsically luminous signal from each type of transient. We take rates from Stone & Metzger (2016), Coppejans et al. (2020), Margutti & Chornock (2021), and Ghirlanda & Salvaterra (2022). For the GRBs, both long and short, we apply a beaming correction assuming a jet opening angle $\sim 3^\circ$. See Table 3 for more details. As with the rest of the paper, the number of expected observations per year is quoted out to $z = 1$, corresponding to $d_L \sim 6700$ Mpc or $d_{\text{com}} \sim 3350$ Mpc. For each class of transient shown here, next-generation instruments (open markers) represent an increase in the anticipated number of events observed per year. In the case of more intrinsically luminous transients, this is due to increased FOV, while less luminous classes benefit more from improved sensitivity (see Figure 8).

3.3. Rates of Transient Discovery

There is a well-known trade-off between instrument FOV and sensitivity, as shown in Figure 7, using specifications from currently operating and proposed missions: larger FOVs tend to correlate with lower sensitivities.

Making the reasonable assumption that we have already observed, and included in our DLPS, the most luminous events from each subclass of transient/variable, we can decouple the advantages of increased FOV and increased sensitivity with transient peak luminosities and volumetric rates from Stone & Metzger (2016), Coppejans et al. (2020), Margutti & Chornock (2021), and Ghirlanda & Salvaterra (2022), separately examining the importance of wide-field instruments and extremely sensitive instruments. For the GRBs (both long and short), we apply a beaming correction factor based on a conservative jet opening angle of $\sim 3^\circ$ (Fong et al. 2015; Rouco Escorial et al. 2022). Calculating the maximum distance out to which each class of transient can be observed based on instrument sensitivity, $d_L = \sqrt{L_{\text{max}}/(4\pi \times \text{sensitivity})}$, we can use a three-dimensional observing volume, defined as $\frac{\text{FOV}}{\Omega} \times \frac{4}{3}\pi d_{\text{com}}^3$ (where FOV is the instrument FOV, Ω is the solid angle of the sky, and d_{com} is the maximum comoving distance out to which each class of transients can be observed inferred from d_L and the cosmology in Section 1), to ascertain the number of anticipated transient observations per year for instruments of varying sensitivity and FOV.

We can isolate the impact of increased FOV by effectively marginalizing oversensitivity and looking at the number of observations as a function of FOV. We choose a representative sensitivity of 10^{-13} erg s $^{-1}$ cm $^{-2}$, corresponding to the median

flux limit of the instruments listed in Table 2, and assume a static pointing, so that the importance of signals serendipitously falling in that FOV is clear. We show this in the left panel of Figure 8. Similarly, we can look at the importance of increased sensitivity by selecting a representative FOV (1 deg 2 , corresponding to the median FOV among instruments in Table 2) and plotting the number of detections per class of transient as a function of sensitivity. This is shown in the right panel of Figure 8. As in the rest of the paper, we limit our events and observing depths to the redshift range in which their rates are well constrained ($z \leq 1$). It is then apparent that, for the detection of bright sources like GRBs, TDEs, SBOs, and FBOTs within $z = 1$, there is little, if anything, to be gained by improving instrument sensitivity beyond a 1 ks flux limit $\sim 10^{-14}$ erg s $^{-1}$ cm $^{-2}$; instead, wide FOV instruments will be critical to the discovery and observation of these events.

We can also use each class’s maximum luminosity along with the instrument sensitivity to determine the distance out to which each transient/variable event can be observed. We take the maximum luminosity of the transient in the GRB, SBO, SN, TDE, CV, magnetar flare/outburst, cool stellar flare, XRB, ULX, FBOT, and FRB categories to represent the most luminous end of their respective distributions. We then apply the 0.3–10 keV flux limit (as in Figure 7 and Table 2) to determine the luminosity distance out to which the transient can be detected, from which we estimate the comoving distance.

For Galactic transients (i.e., CVs, magnetar flares/outbursts, and cool stellar flares) and Galactic/extragalactic transients (i.e., XRBs, ULXs, and FRBs²⁶), we show the luminosity

²⁶ Though the only FRB with an apparent X-ray counterpart (FRB 200428) is a Galactic source, the population of observed FRBs is largely extragalactic.

Table 3
Estimated Rate (in yr⁻¹) of Serendipitous Detections of Extragalactic Transients in a Single Pointing of Each Soft X-Ray Instrument

Instrument	sGRBs	IGRBs	SNe	SLSNe	Nonthermal TDEs	Thermal TDEs	SBOs	FBOTs
ROSAT	6.28 × 10 ⁻³ 8.98 × 10 ⁻¹¹	5.34 × 10 ⁻³ 2.19 × 10 ⁻⁶	0.13 6.32 × 10 ⁻¹³	6.63 × 10 ⁻⁴ 9.96 × 10 ⁻⁷	1.15 × 10 ⁻⁴ 8.28 × 10 ⁻⁸	1.15 × 10 ⁻² 1.59 × 10 ⁻¹²	7.74 2.85 × 10 ⁻²	1.00 3.62 × 10 ⁻⁸
Chandra	1.66 × 10 ⁻⁴ 1.25 × 10 ⁻¹¹	1.41 × 10 ⁻⁴ 2.73 × 10 ⁻⁷	1.69 × 10 ⁻² 8.81 × 10 ⁻¹⁴	8.35 × 10 ⁻⁵ 1.37 × 10 ⁻⁷	3.03 × 10 ⁻⁶ 1.01 × 10 ⁻⁸	3.03 × 10 ⁻⁴ 2.22 × 10 ⁻¹³	0.68 3.57 × 10 ⁻³	7.86 × 10 ⁻² 5.04 × 10 ⁻⁹
Swift/XRT	3.24 × 10 ⁻⁴ 1.64 × 10 ⁻¹²	2.75 × 10 ⁻⁴ 4.18 × 10 ⁻⁸	2.49 × 10 ⁻³ 1.15 × 10 ⁻¹⁴	1.26 × 10 ⁻⁵ 1.83 × 10 ⁻⁸	5.91 × 10 ⁻⁶ 1.60 × 10 ⁻⁹	5.91 × 10 ⁻⁴ 2.91 × 10 ⁻¹⁴	0.18 5.43 × 10 ⁻⁴	2.46 × 10 ⁻² 6.62 × 10 ⁻¹⁰
MAXI GSC	1.00 5.35 × 10 ⁻¹³	0.854 1.53 × 10 ⁻⁸	8.81 × 10 ⁻⁴ 3.68 × 10 ⁻¹⁵	4.55 × 10 ⁻⁶ 6.01 × 10 ⁻⁹	1.83 × 10 ⁻² 5.98 × 10 ⁻¹⁰	2.21 × 10 ⁻³ 9.46 × 10 ⁻¹⁵	0.12 1.97 × 10 ⁻⁴	2.24 × 10 ⁻² 2.16 × 10 ⁻¹⁰
MAXI SSC	0.283 4.54 × 10 ⁻¹⁴	0.240 1.39 × 10 ⁻⁹	7.49 × 10 ⁻⁵ 3.23 × 10 ⁻¹⁶	3.87 × 10 ⁻⁷ 5.10 × 10 ⁻¹⁰	5.16 × 10 ⁻³ 5.09 × 10 ⁻¹¹	2.02 × 10 ⁻⁴ 8.03 × 10 ⁻¹⁶	1.01 × 10 ⁻² 1.68 × 10 ⁻⁵	.95 × 10 ⁻³ 1.83 × 10 ⁻¹¹
XMM-Newton	4.40 × 10 ⁻⁴ 3.81 × 10 ⁻¹¹	3.74 × 10 ⁻⁴ 8.22 × 10 ⁻⁷	5.10 × 10 ⁻² 2.69 × 10 ⁻¹³	2.52 × 10 ⁻⁴ 4.19 × 10 ⁻⁷	8.02 × 10 ⁻⁶ 3.04 × 10 ⁻⁸	8.02 × 10 ⁻⁴ 6.79 × 10 ⁻¹³	2.00 1.08 × 10 ⁻²	0.23 1.54 × 10 ⁻⁸
eROSITA	2.09 × 10 ⁻³ 2.99 × 10 ⁻¹¹	1.78 × 10 ⁻³ 7.29 × 10 ⁻⁷	4.39 × 10 ⁻² 2.11 × 10 ⁻¹³	2.21 × 10 ⁻⁴ 3.32 × 10 ⁻⁷	3.82 × 10 ⁻⁵ 2.76 × 10 ⁻⁸	3.82 × 10 ⁻³ 5.31 × 10 ⁻¹³	2.58 9.49 × 10 ⁻³	0.334 1.21 × 10 ⁻⁸
NICER	1.74 × 10 ⁻⁵ 3.48 × 10 ⁻¹³	1.48 × 10 ⁻⁵ 8.33 × 10 ⁻⁹	5.04 × 10 ⁻⁴ 2.45 × 10 ⁻¹⁵	2.53 × 10 ⁻⁶ 3.86 × 10 ⁻⁹	3.18 × 10 ⁻⁷ 3.14 × 10 ⁻¹⁰	3.18 × 10 ⁻⁵ 6.19 × 10 ⁻¹⁵	2.77 × 10 ⁻² 1.09 × 10 ⁻⁴	3.51 × 10 ⁻³ 1.41 × 10 ⁻¹⁰
Insight-HXMT/LE	1.70 1.33 × 10 ⁻¹¹	1.44 3.76 × 10 ⁻⁷	2.17 × 10 ⁻² 9.25 × 10 ⁻¹⁴	1.12 × 10 ⁻⁴ 1.49 × 10 ⁻⁷	3.09 × 10 ⁻² 1.47 × 10 ⁻⁸	4.12 × 10 ⁻² 2.35 × 10 ⁻¹³	2.73 4.85 × 10 ⁻³	0.50 5.35 × 10 ⁻⁹
SVOM/MXT	2.38 × 10 ⁻³ 1.35 × 10 ⁻¹³	2.03 × 10 ⁻³ 3.78 × 10 ⁻⁹	2.19 × 10 ⁻⁴ 9.50 × 10 ⁻¹⁶	1.13 × 10 ⁻⁶ 1.52 × 10 ⁻⁹	4.35 × 10 ⁻⁵ 1.47 × 10 ⁻¹⁰	1.73 × 10 ⁻⁴ 2.39 × 10 ⁻¹⁵	2.52 × 10 ⁻² 4.89 × 10 ⁻⁵	4.38 × 10 ⁻³ 5.46 × 10 ⁻¹¹
XRISM/Xtend	8.40 × 10 ⁻⁴ 2.58 × 10 ⁻¹¹	7.14 × 10 ⁻⁴ 6.01 × 10 ⁻⁷	3.66 × 10 ⁻² 1.82 × 10 ⁻¹³	1.83 × 10 ⁻⁴ 2.85 × 10 ⁻⁷	1.53 × 10 ⁻⁵ 2.26 × 10 ⁻⁸	2.94 × 10 ⁻⁴ 2.39 × 10 ⁻¹⁵	1.83 7.84 × 10 ⁻³	0.22 1.04 × 10 ⁻⁸
Athena WFI	9.31 × 10 ⁻⁴ 3.50 × 10 ⁻⁸	7.91 × 10 ⁻⁴ 2.55 × 10 ⁻⁴	19.5 2.65 × 10 ⁻¹⁰	8.49 × 10 ⁻² 3.38 × 10 ⁻⁴	1.70 × 10 ⁻⁵ 8.20 × 10 ⁻⁶	1.70 × 10 ⁻³ 6.58 × 10 ⁻¹⁰	12.0 3.46	0.51 1.42 × 10 ⁻⁵
eXTP/WFM	33.9 1.80 × 10 ⁻¹¹	28.8 5.16 × 10 ⁻⁷	2.97 × 10 ⁻² 1.24 × 10 ⁻¹³	1.53 × 10 ⁻⁴ 2.03 × 10 ⁻⁷	0.62 2.02 × 10 ⁻⁸	7.46 × 10 ⁻² 3.19 × 10 ⁻¹³	3.97 6.66 × 10 ⁻³	0.76 7.28 × 10 ⁻⁹
AXIS	2.63 × 10 ⁻⁴ 3.75 × 10 ⁻⁸	2.24 × 10 ⁻⁴ 1.77 × 10 ⁻⁴	14.4 2.96 × 10 ⁻¹⁰	6.03 × 10 ⁻² 3.37 × 10 ⁻⁴	4.80 × 10 ⁻⁶ 4.80 × 10 ⁻⁶	4.80 × 10 ⁻⁴ 7.28 × 10 ⁻¹⁰	3.38 2.42	0.14 1.53 × 10 ⁻⁵
Einstein Probe/WXT	7.54 3.83 × 10 ⁻¹¹	6.41 1.09 × 10 ⁻⁶	6.28 × 10 ⁻² 2.68 × 10 ⁻¹³	3.24 × 10 ⁻⁴ 4.30 × 10 ⁻⁷	0.14 4.24 × 10 ⁻⁸	0.13 6.77 × 10 ⁻¹³	7.99 1.40 × 10 ⁻²	1.48 1.54 × 10 ⁻⁸
STAR-X	2.09 × 10 ⁻³ 1.81 × 10 ⁻¹⁰	1.78 × 10 ⁻³ 3.91 × 10 ⁻⁶	0.24 1.28 × 10 ⁻¹²	1.20 × 10 ⁻³ 1.99 × 10 ⁻⁶	3.82 × 10 ⁻⁵ 1.45 × 10 ⁻⁷	3.82 × 10 ⁻³ 3.23 × 10 ⁻¹²	9.50 5.13 × 10 ⁻²	1.08 7.32 × 10 ⁻⁸
STROBE-X	7.31 × 10 ⁻⁶ 2.95 × 10 ⁻¹³	6.21 × 10 ⁻⁶ 6.75 × 10 ⁻⁹	4.13 × 10 ⁻⁴ 2.08 × 10 ⁻¹⁵	2.06 × 10 ⁻⁶ 3.26 × 10 ⁻⁹	1.33 × 10 ⁻⁷ 2.52 × 10 ⁻¹⁰	1.33 × 10 ⁻⁵ 5.24 × 10 ⁻¹⁵	1.94 × 10 ⁻² 8.81 × 10 ⁻⁵	2.34 × 10 ⁻³ 1.19 × 10 ⁻¹⁰
Lynx/HDXI	2.82 × 10 ⁻⁴ 2.62 × 10 ⁻⁵	2.39 × 10 ⁻⁴ 2.39 × 10 ⁻⁴	36.2 4.85 × 10 ⁻⁷	0.10 9.97 × 10 ⁻²	5.14 × 10 ⁻⁶ 5.14 × 10 ⁻⁶	5.14 × 10 ⁻⁴ 9.33 × 10 ⁻⁷	3.62 3.62	0.15 1.13 × 10 ⁻²
THESEUS/SXI	6.51 3.31 × 10 ⁻¹¹	5.54 9.39 × 10 ⁻⁷	5.43 × 10 ⁻² 2.32 × 10 ⁻¹³	2.80 × 10 ⁻⁴ 3.71 × 10 ⁻⁷	0.12 3.67 × 10 ⁻⁸	0.11 5.85 × 10 ⁻¹³	6.90 1.21 × 10 ⁻²	1.28 1.33 × 10 ⁻⁸

Note. For each instrument we show an upper (top) and lower (bottom) limit for the serendipitous observation rate, assuming that the instrument remains pointed at the same portion of the sky and takes 1 ks exposures. The upper limit is based on the observing volume calculated for the most luminous observation of an event in that class, while the lower limit is based on the observing volume calculated for the least luminous observation of an event in that class. As in Table 2, we separate past, present, planned, and proposed instruments with horizontal lines.

distance out to which various transients can be observed versus the fraction of the sky covered instantaneously by the instrument FOV in Figure 9. As in the rest of this work, we limit instrument depth to a maximum luminosity distance that corresponds to $z = 1$. Needless to say, the qualitative trends captured by our Galactic and Galactic/extragalactic transient observing volume plot (Figure 9) translate to the behavior of exclusively extragalactic sources, with targeted instruments being more conducive to observing distant phenomena, while wide-field instruments have considerably shallower sky coverage.

For extragalactic transients (i.e., GRBs, SBOs, SNe, FBOTs, TDEs, and AGNs), we instead examine an estimate of the number of observed events per year for each class of phenomena broken down by instrument. Using the three-dimensional observing volumes for each instrument included in Table 2 and the same volumetric rates as in Figure 8, we construct Figure 10. The rates shown in Figure 10 are upper

limits based on the most luminous event in each class. In Table 3, we report these upper limits in addition to lower limits (based on the least luminous observation in each extragalactic class in our DLPS). Both Figure 10 and Table 3 report anticipated serendipitous detection rates, assuming that the instrument maintains a single static pointing on the sky and that each transient is observed as it undergoes a flare. This allows us to more readily compare instrument specifications without accounting for observing strategy. In reality, the observed rates may be much higher, particularly for survey instruments and classes of transient that can be observed months after the initial outburst (e.g., Sazonov et al. 2021).

4. Conclusion

With the immense promise of next-generation X-ray instruments on the horizon and community investment in large time-domain surveys, many more X-ray transients will be

detected and studied in the coming years. We constructed a set of observational X-ray phase space plots from 284 light curves of 221 objects, which show distinctions between different transient and variable phenomena and highlight the luminosity evolution of these events. We included light curves of GRB afterglows, SNe, SBOs, TDEs and AGNs, FBOTs, CVs, magnetar flares/outbursts and FRBs, cool stellar flares, XRB outbursts, and ULXs composed of observations from a range of telescopes (see Table 1 for a full list). The X-ray DLPS can be used to help disambiguate the nature of newly observed signals by placing them in context (even before spectroscopic or multiwavelength follow-up, as demonstrated in Section 3.1) and to point out sparse areas of the phase space that should be the focus of future exploration.

As expected, the phase space is less populated at extremely low luminosities and extremely short durations, given the limitations of current instruments and the trade-off between FOV and sensitivity in instrument design. More sensitive imagers will provide better insight into less luminous events, but wide-field imagers will be necessary to serendipitously capture the most ephemeral signals, like those of candidate FRB counterparts. There is another, less intuitive gap in the phase space around $L_X = 10^{34} - 10^{42}$ erg s⁻¹ and duration 10⁻⁴ to 0.1 days. We expect this part of the X-ray phase space to include both SBOs and magnetar flares, both of which are classes of transient that have a relative paucity of observations. Additional observations targeting this part of the phase space will not only increase the studied population of known classes of transient but potentially uncover yet-unidentified signals as well.

Acknowledgments

The authors thank the anonymous referees for comments and suggestions that significantly improved the manuscript, as well

as Laura Chomiuk, Irina Zhuravleva, and Magaretha Pretorius for helpful discussions. A.P. thanks Andrey Kravtsov for the suggestion to make a preliminary classifier available. K.L.P. acknowledges support from the UK Space Agency. This work made use of data supplied by the UK Swift Science Data Centre at the University of Leicester. R.M. acknowledges partial support by the National Science Foundation under grant Nos. AST-2221789 and AST-2224255 and by the Heising-Simons Foundation under grant No. 2021-3248. G.V. acknowledges support by the Hellenic Foundation for Research and Innovation (H.F.R.I.) under the “3rd Call for H.F.R.I. Research Projects to support Postdoctoral Researchers” through the project ASTRAPE (Project ID 7802).

This research has made use of MAXI data provided by RIKEN, JAXA, and the MAXI team.

Software: AstroPy (Astropy Collaboration et al. 2013, 2018), Matplotlib (Hunter 2007), NumPy (Harris et al. 2020), pandas (McKinney 2010; pandas development team 2020), PIMMS (Mukai 1993), scikit-learn (Pedregosa et al. 2011), SciPy (Virtanen et al. 2020), WebPlotDigitizer (Rohatgi 2019), xraydlps (Polzin et al. 2023).

Appendix A Data

We list in Tables A1–A10 all of the events included in the paper. For each event, we also provide coordinates, distance, and references, and, where applicable, we provide subclassification. For GRBs, we also list redshift and T_{90} . These data are available on GitHub (see Section 2), with a few limited exceptions, which are marked clearly in the tables below. Quoted distances are luminosity distances for the cosmology indicated in Section 1.

Table A1
Gamma-Ray Bursts

Name	Type	T_{90} (s)	R.A.	Decl.	z	Distance (kpc)	References
GRB 980425A	subluminous	22.0	19:35:03	-52:50:46	0.0085	2.7×10^4	Pian et al. (2000), Kouveliotou et al. (2004)
GRB 031203A	subluminous	30	08:02:30	-39:51:03	0.105	4.9×10^5	Sazonov et al. (2004), Watson et al. (2004)
GRB 050509B	short	0.073	12:36:18	+29:01:24	0.225	1.1×10^6	Evans et al. (2007, 2009)
GRB 050724	short	3.00	16:24:44	-27:32:28	0.258	1.3×10^6	Evans et al. (2007, 2009)
GRB 051221A	short	1.400	21:54:49	+16:53:27	0.5465	3.2×10^6	Evans et al. (2007, 2009)
GRB 060218A	subluminous	2100	09:09:31	+33:08:20	0.0331	1.5×10^5	Evans et al. (2007, 2009)
GRB 061006	short	0.42	07:24:08	-79:11:55	0.438	2.4×10^6	Evans et al. (2007, 2009)
GRB 061210	short	85.0	09:38:05	+15:37:17	0.4095	2.3×10^6	Evans et al. (2007, 2009)
GRB 061217	short	0.210	10:41:39	-21:07:22	0.827	5.3×10^6	Evans et al. (2007, 2009)
GRB 070714B	short	3.0	03:51:22	+28:17:51	0.923	6.1×10^6	Evans et al. (2007, 2009)
GRB 070724A	short	0.4	01:51:14	-18:35:39	0.457	2.6×10^6	Evans et al. (2007, 2009)
GRB 071227	short	1.8	03:52:31	-55:59:03	0.383	2.1×10^6	Evans et al. (2007, 2009)
GRB 080905A	short	1.0	19:10:39	-18:51:55	0.1218	5.7×10^5	Evans et al. (2007, 2009)
GRB 090510A	short	0.3	22:14:13	-26:35:51	0.903	5.9×10^6	Evans et al. (2007, 2009)
GRB 100117A	short	0.3	00:45:05	-01:35:42	0.92	6.0×10^6	Evans et al. (2007, 2009)
GRB 100316D	subluminous	292.8	07:10:31	-56:15:20	0.059	2.7×10^5	Evans et al. (2007, 2009)
GRB 100816A	short	2.9	23:26:58	+26:34:43	0.8049	5.1×10^6	Evans et al. (2007, 2009)
GRB 101219A	short	0.6	04:58:20	-02:32:23	0.718	4.4×10^6	Evans et al. (2007, 2009)
GRB 101225A	ultralong	1088	00:00:47	+44:36:01	0.847	5.5×10^6	Evans et al. (2007, 2009)
GRB 141212A	short	0.30	02:36:30	+18:08:49	0.596	3.5×10^6	Evans et al. (2007, 2009)
GRB 141225A	long	40.24	09:15:07	+33:47:31	0.915	6.0×10^6	Evans et al. (2007, 2009)
GRB 150101B	short	0.08	12:32:05	-10:56:01	0.134	6.4×10^5	Evans et al. (2007, 2009)
GRB 150323A	long	149.6	08:32:43	+45:27:53	0.593	3.5×10^6	Evans et al. (2007, 2009)
GRB 150514A	long	10.8	04:59:30	-60:58:07	0.807	5.1×10^6	Evans et al. (2007, 2009)
GRB 150518A	subluminous	...	15:36:48	+16:19:47	0.256	1.3×10^6	Evans et al. (2007, 2009)
GRB 150727A	long	88	13:35:53	-18:19:32	0.313	1.6×10^6	Evans et al. (2007, 2009)
GRB 150818A	long	123.3	15:21:25	+68:20:31	0.282	1.5×10^6	Evans et al. (2007, 2009)
GRB 150821A	long	172.1	22:47:39	-57:53:38	0.755	4.7×10^6	Evans et al. (2007, 2009)
GRB 151027A	long	129.69	18:09:57	+61:21:12	0.81	5.2×10^6	Evans et al. (2007, 2009)
GRB 160131A	long	325	05:12:40	-07:03:00	0.972	6.5×10^6	Evans et al. (2007, 2009)
GRB 160314A	long	8.73	07:31:10	+16:59:57	0.726	4.9×10^6	Evans et al. (2007, 2009)
GRB 160425A	long	304.58	18:41:19	-54:21:36	0.555	3.2×10^6	Evans et al. (2007, 2009)
GRB 160623A	long	13.5	21:01:12	+42:13:15	0.367	2.0×10^6	Evans et al. (2007, 2009)
GRB 160624A	short	0.2	22:00:46	+29:38:38	0.483	2.7×10^6	Evans et al. (2007, 2009)
GRB 160804A	long	130	14:46:31	+09:59:56	0.736	4.6×10^3	Evans et al. (2007, 2009)
GRB 160821B	short	0.48	18:39:55	+62:23:30	0.16	7.7×10^5	Evans et al. (2007, 2009)
GRB 161129A	long	35.53	21:04:55	+32:08:05	0.645	3.9×10^6	Evans et al. (2007, 2009)
GRB 161219B	long	6.94	06:06:5	-26:47:30	0.1475	7.1×10^5	Evans et al. (2007, 2009)
GRB 170519A	long	216.4	10:53:42	+25:22:27	0.818	5.2×10^6	Evans et al. (2007, 2009)
GRB 170607A	long	23.0	00:29:28	+09:14:36	0.557	3.3×10^6	Evans et al. (2007, 2009)
GRB 170714A	ultralong	1000	02:17:24	+01:59:29	0.793	5.0×10^6	Evans et al. (2007, 2009)
GRB 170817A	short	2.0	13:09:48	-23:22:53	0.0099	4.3×10^4	Hajela et al. (2019, 2020)
GRB 171010A	long	70.3	04:26:19	-10:27:48	0.3285	1.7×10^6	Evans et al. (2007, 2009)
GRB 171205A	subluminous	189.4	11:09:39	-12:35:19	0.0368	1.6×10^5	Evans et al. (2007, 2009)
GRB 180404A	long	35.2	05:34:12	-37:10:05	1.000	6.7×10^6	Evans et al. (2007, 2009)
GRB 180703A	long	20.9	00:24:28	-67:18:18	0.6678	4.0×10^6	Evans et al. (2007, 2009)
GRB 180720B	long	51.1	00:02:07	-02:55:08	0.654	4.0×10^6	Evans et al. (2007, 2009)
GRB 180728A	long	8.68	16:54:16	-54:02:40	0.117	5.5×10^5	Evans et al. (2007, 2009)
GRB 190114C	long	361.5	03:38:01	-26:56:48	0.425	2.4×10^6	Evans et al. (2007, 2009)
GRB 190829A	long	63	02:58:10	-08:57:30	0.0785	3.6×10^5	Evans et al. (2007, 2009)
GRB 191019A	long	64.35	22:40:06	-17:19:41	0.248	1.3×10^6	Evans et al. (2007, 2009)
GRB 221009A	long	327	19:12:50	+19:43:48	0.151	7.2×10^5	Evans et al. (2007, 2009), de Ugarte Postigo et al. (2022)

Table A2
Shock Breakouts

Name	Type	R.A.	Decl.	Distance (kpc)	References
GRB 980425A	stellar surface	19:35:03	−52:50:46	3.7×10^4	Pian et al. (2000), Kouveliotou et al. (2004)
GRB 031203A	stellar surface	08:02:30	−39:51:03	4.9×10^5	Sazonov et al. (2004), Watson et al. (2004)
GRB 060218A	stellar surface	03:21:40	+16:52:02	1.5×10^5	Evans et al. (2007, 2009)
SN 2008D (GRB 080109A)	wind	09:09:31	+33:08:20	2.7×10^4	Soderberg et al. (2008)
GRB 100316D	stellar surface	07:10:31	−56:15:20	2.7×10^5	Evans et al. (2007, 2009)
GRB 150518A	stellar surface	15:36:48	+16:19:47	1.3×10^6	Evans et al. (2007, 2009)
GRB 171205A	stellar surface	11:09:39	−12:35:19	1.6×10^5	Evans et al. (2007, 2009)

Note. Subluminous GRBs are considered candidates for stellar surface SBOs. We include them here under that assumption.

Table A3
Supernovae

Name	Type	R.A.	Decl.	Distance (kpc)	References
SN 1978K	II	03:17:39	−66:33:03	4.5×10^3	R. Margutti (2023, private communication)
SN 1981K	II	12:18:59	+47:19:31	7.2×10^3	Immler et al. (2007c)
SN 1987A	IIPec	05:35:28	−69:16:11	50	Haberl et al. (2006), Heng et al. (2008), Sturm et al. (2010)
SN 1993J	IIfb	09:55:25	+69:01:14	2.6×10^3	Chandra et al. (2009)
SN 1995N	IIn	14:49:28	−10:10:14	2.4×10^4	Zampieri et al. (2005)
SN 1996cr	IIn	14:13:10	−65:20:45	3.8×10^3	Bauer et al. (2008)
SN 1998bw	Ib/c	19:35:03	−52:50:46	3.8×10^4	Kouveliotou et al. (2004)
SN 1999em	IIP	04:41:27	−02:51:45	7.8×10^3	Pooley et al. (2002)
SN 1999gi	IIP	10:18:17	+41:26:28	8.7×10^3	Schlegel (2001)
SN 2001ig	II	22:57:31	−41:02:26	1.1×10^4	Schlegel & Ryder (2002)
SN 2002ap	Ib/c	01:36:24	+15:45:13	1.0×10^4	Soria et al. (2004)
SN 2003bg	Ic/pec	04:10:59	−31:24:50	1.9×10^4	Soderberg et al. (2006)
SN 2004et	II	20:35:25	+60:07:18	5.5×10^3	Misra et al. (2007)
SN 2005ip	IIn	09:32:06	+08:26:44	3.0×10^4	Immler & Pooley (2007)
SN 2005kd	IIn	04:03:17	+71:43:19	6.4×10^4	Immler et al. (2007d), Pooley et al. (2007)
SN 2006bp	IIP	11:53:56	+52:21:09	1.5×10^4	Immler et al. (2007b)
SN 2006jc	Ibc	09:17:21	+41:54:33	2.4×10^4	Immler et al. (2008)
SN 2006jd	IIf/IIn	08:02:07	+00:48:32	7.9×10^4	Immler et al. (2007a)
SN 2007pk	IIn	01:31:47	+33:36:54	7.1×10^4	Immler et al. (2007e)
SN 2008M	II	06:21:41	−59:43:45	3.7×10^4	Immler (2010)
SN 2008ax	IIf	12:30:41	+41:38:16	8.0×10^3	Roming et al. (2009)
SN 2008ij	II	18:19:52	+74:33:55	2.1×10^4	Immler et al. (2009)
SN 2009gj	IIf	00:30:29	−33:12:56	1.8×10^4	Immler & Russell (2009)
SN 2009mk	IIf	00:06:21	−41:29:00	2.1×10^4	Russell & Immler (2010)
SN 2010F	II	10:05:21	−34:13:21	3.9×10^4	Russell et al. (2010)
SN 2010jl	IIn	09:42:53	+09:29:42	4.9×10^4	Immler et al. (2010), Chandra et al. (2015)
SN 2011dh	IIf	13:30:05	+47:10:11	7.3×10^3	Soderberg et al. (2012)
SN 2011ja	IIP	13:05:11	−49:31:27	3.0×10^3	Chakraborti et al. (2013)
SN 2013by	IIf/IIn	16:59:02	−60:11:42	1.5×10^4	Margutti et al. (2013)
SN 2013ej	IIP/IIf	01:36:48	+15:45:31	9.6×10^3	Chakraborti et al. (2016)
SN 2014C	Ib/IIn	22:37:06	+34:24:32	1.5×10^4	Brethauer et al. (2022)
SN 2018gk	IIf/SL	16:35:54	+40:01:58	1.4×10^5	Bose et al. (2021)
SN 2018bsz ^a	I/SL	16:09:39	−32:03:46	1.1×10^5	D. Matthews et al. (2023, in preparation)
SN 2019ehk	Ca-rich	12:22:56	+15:49:34	1.6×10^4	Jacobson-Galán et al. (2020)
SN 2021gno	Ca-rich	12:12:10	+13:14:57	3.05×10^4	Jacobson-Galán et al. (2022)

Notes. Type “SL” denotes superluminous SNe. Additional X-ray SN observations may be, or may become, available in SNaX (kronos.uchicago.edu/snax; Ross & Dwarkadas 2017; Nisenoff et al. 2020), which is a moderated database serving as a repository for user-uploaded X-ray observations of SNe.

^a These data are not shared in the GitHub repository.

Table A4
Tidal Disruption Events and Active Galactic Nuclei

Name	Type	R.A.	Decl.	Distance (kpc)	References
PKS 2155–304	AGN	21:58:52.	−30:13:32	5.4×10^5	Auchettl et al. (2018)
3C 273	AGN	12:29:07	+02:03:09	7.6×10^5	Auchettl et al. (2018)
NGC 4395	AGN	12:25:49	+33:32:49	4.7×10^3	Auchettl et al. (2018)
3C 279	AGN	12:56:11	−05:47:22	3.1×10^6	Auchettl et al. (2018)
3C 345	AGN	16:42:59	+39:48:37	3.5×10^6	Auchettl et al. (2018)
MKN 335	AGN	00:06:20	+20:12:11	1.1×10^5	Auchettl et al. (2018)
CGC 229-10 (Zw 299-015)	AGN	16:41:09	+61:19:35	8.7×10^4	Auchettl et al. (2018)
PS10jh	thermal TDE	16:09:28	+53:40:23	8.2×10^5	Auchettl et al. (2017)
ASASSN-14ae	thermal TDE	11:08:40	+34:05:52	2.0×10^5	Auchettl et al. (2017)
ASASSN-14li	thermal TDE	12:48:15	+17:46:26	9.0×10^4	Miller et al. (2015), Brown et al. (2017) Auchettl et al. (2017), Bright et al. (2018)
ASASSN-15oi	thermal TDE	20:39:09	−30:45:21	2.2×10^5	Auchettl et al. (2017), Holoien et al. (2018)
Swift 1644+57	nonthermal TDE	16:44:49	+57:34:51	1.9×10^6	Mangano et al. (2016), Auchettl et al. (2017)
ASASSN-19bt	nonthermal TDE	07:00:11	−66:02:25	1.15×10^5	Holoien et al. (2019)
Swift J2058.4+0516 ^a	nonthermal TDE	20:58:20	+05:13:32	1×10^7	Auchettl et al. (2017)
SDSS J131122.15−012345.6	thermal TDE	13:11:22	−01:23:46	9.0×10^5	Auchettl et al. (2017)
SDSS J132341.97+482701.3	thermal TDE	13:23:42	+48:27:01	4.0×10^5	Auchettl et al. (2017)
SDSS J1201+3003	thermal TDE	12:01:36	+30:03:06	7.1×10^5	Auchettl et al. (2017)
WINGS J1348	thermal TDE	13:48:51	+26:35:06	2.8×10^5	Auchettl et al. (2017)
RBS 1032	thermal TDE	11:47:27	+49:42:57	1.1×10^5	Auchettl et al. (2017)
3XMM J1521+0749	thermal TDE	11:47:27	+49:42:58	8.9×10^5	Auchettl et al. (2017)
GSN 069	AGN/QPE	01:19:09	−34:11:30	7.86×10^4	Miniutti et al. (2019)
2MASX J0249	thermal TDE	02:49:17	−04:12:52	8.0×10^4	Auchettl et al. (2017)
IGR J17361−4441	thermal TDE	17:36:17	−44:44:06	1.8×10^5	Auchettl et al. (2017)
NGC 247	thermal TDE	00:47:09	−20:45:37	2240	Auchettl et al. (2017)
OGLE 16aaa	thermal TDE	01:07:21	−64:16:21	8.1×10^5	Auchettl et al. (2017)
PTF-10iya	thermal TDE	14:38:41	+37:39:33	1.2×10^6	Auchettl et al. (2017)
XMMSL1 J0740−85	thermal TDE	07:40:08	−85:39:31	7.4×10^4	Auchettl et al. (2017)

Note.

^a Though Swift J2058.4+0516 is at $z \sim 1$, we include its light curve anyway owing to the relative paucity of nonthermal TDE observations and the uncertainty on its distance estimate.

Table A5
Fast Blue Optical Transients

Name	R.A.	Decl.	Distance (kpc)	References
CSS 161010	04:58:34	−08:18:04	1.5×10^5	Coppejans et al. (2020)
AT 2018cow	16:16:00	+22:16:05	6.0×10^4	Margutti et al. (2019)
AT 2020xnd	22:20:02	−02:50:25	1.2×10^6	Bright et al. (2022)
AT 2020mrf	15:47:54	+44:29:07	6.37×10^5	Yao et al. (2022)
AT 2022tsd	03:20:11	+08:44:56	1.3×10^6	Schulze et al. (2022), Matthews et al. (2022), Matthews & Margutti (2023)

Table A6
Cataclysmic Variables

Name	Type	R.A.	Decl.	Distance (kpc)	References
V838 Her	Nova	18:46:32	+12:14:01	3.4	Mukai et al. (2008)
V1974 Cyg	Nova	20:30:32	+52:37:51	1.9	Mukai et al. (2008)
V351 Pup	Nova	08:11:38	-35:07:30	4.7	Mukai et al. (2008)
V382 Vel	Nova	10:44:48	-52:25:31	1.7	Mukai et al. (2008)
N LMC 2000 ^a	Nova	05:25:02	-70:14:17	55	Mukai et al. (2008)
V4633 Sgr	Nova	18:21:40	-27:31:37	8.9	Mukai et al. (2008)
V5116 Sgr	Nova	18:17:51	-30:26:31	11.3	Mukai et al. (2008)
V1663 Aql	Nova	19:05:12	+05:14:12	5.5	Mukai et al. (2008)
V477 Sct	Nova	18:38:43	-12:16:16	11	Mukai et al. (2008)
V382 Nor	Nova	16:19:45	-51:34:53	13.8	Mukai et al. (2008)
RS Oph	Nova	17:50:13	-06:42:28	1.6	Page et al. (2020)
V2362 Cyg	Nova	21:11:32	+44:48:04	7.2–15.8	Poggiani (2009), Page et al. (2020)
V1280 Sco	Nova	16:57:41	-32:20:36	1.6	Chesneau et al. (2008), Page et al. (2020)
V1281 Sco	Nova	16:56:59	-35:21:50	25.9	Kantharia (2017), Page et al. (2020)
V458 Vul	Nova	19:54:25	+20:52:53	8.5	Page et al. (2020)
V597 Pup	Nova	08:16:18	-34:15:25	3	Worpel et al. (2020), Page et al. (2020)
V2468 Cyg	Nova	19:58:34	+29:52:12	5.6	Raj et al. (2015), Page et al. (2020)
V2491 Cyg	Nova	19:43:02	+32:19:14	10.5–14	Darnley et al. (2011), Page et al. (2020)
HV Cet (CSS 081007)	Nova	03:05:59	+05:47:16	4.45	Page et al. (2020)
LMC 2009a	Nova	05:04:44	-66:40:12	50	Page et al. (2020)
V2672 Oph	Nova	17:38:20	-26:44:14	19	Munari et al. (2011), Page et al. (2020)
KT Eri	Nova	04:47:54	-10:10:43	6.3	Raj et al. (2013), Page et al. (2020)
U Sco	Nova	16:22:31	-17:52:43	12	Schaefer (2010), Page et al. (2020)
V407 Cyg	Nova	21:02:10	+45:46:33	2.7	Page et al. (2020)
T Pyx	Nova	09:04:42	-32:22:48	3.185	Schaefer (2018), Page et al. (2020)
LMC 2012	Nova	04:54:57	-70:26:56	50	Page et al. (2020)
V959 Mon	Nova	06:39:39	+05:53:53	1.4	Page et al. (2020), Li et al. (2020a)
SMC 2012	Nova	00:32:34	-74:20:15	61	Page et al. (2020)
V339 Del	Nova	20:23:31	+20:46:04	2.1	Page et al. (2020), Li et al. (2020a)
V1369 Cen	Nova	13:54:45	-59:09:04	2.0	Page et al. (2020), Li et al. (2020a)
V745 Sco	Nova	17:55:22	-33:14:59	7.8	Schaefer (2010), Page et al. (2020)
V1534 Sco	Nova	17:15:47	-31:28:30	8.8	Hachisu & Kato (2018), Page et al. (2020)
V1535 Sco	Nova	17:03:26	-35:04:18	8.5	Linford et al. (2017), Page et al. (2020)
V5668 Sgr	Nova	18:37:40	-29:04:03	2.0	Page et al. (2020), Li et al. (2020a)
LMC 1968-12a	Nova	05:09:58	-71:39:53	50	Page et al. (2020)
V407 Lup	Nova	15:29:02	-44:49:41	~10	Aydi et al. (2018), Page et al. (2020)
SMCN 2016-10a	Nova	01:06:03	-74:47:16	61	Page et al. (2020)
V549 Vel	Nova	08:50:30	-47:45:28	0.560	Page et al. (2020), Li et al. (2020a)
SS Cyg	Dwarf Nova	21:42:43	+43:35:10	0.115	Wheatley et al. (2003), McGowan et al. (2004), Pala et al. (2020)
GW Lib	Dwarf Nova	15:19:55	-25:00:25	0.113	Byckling et al. (2009), Neustroev et al. (2018), Pala et al. (2020)
SSS J122221.7–311525	Dwarf Nova	12:22:22	-31:15:24	0.275	Neustroev et al. (2018)

Notes. We include only the dwarf novae with well-observed X-ray brightening during their optical outbursts.

^a We quote the 55 kpc distance assumed by Mukai et al. (2008) since these light curves are from that paper and presented as luminosity versus time. Other novae in the LMC are listed with a more recently revised distance (Pietrzyński et al. 2013), as those data were initially presented as flux versus time.

Table A7
Magnetar Flares/Outbursts + FRBs

Name	Type	R.A.	Decl.	Distance (kpc)	References
1E 161348–5055	Outburst	16:17:33	−51:02:00	3.3	Rea et al. (2016), Esposito et al. (2019)
SGR 1627–41	Outburst	16:35:52	−47:35:12	11	Coti Zelati et al. (2018)
1E 2259+586	Outburst	23:01:08	+58:52:44	3.2	Coti Zelati et al. (2018)
XTE J1810–197	Outburst	18:09:51	−19:43:52	3.5	Coti Zelati et al. (2018)
SGR 1806–20	Outburst	18:08:39	−20:24:40	8.7	Coti Zelati et al. (2018)
CXOU J1647–4552	Outburst	16:47:10	−45:52:17	4	Coti Zelati et al. (2018)
SGR 0501+4516	Outburst	05:01:08	+45:16:31	1.5	Coti Zelati et al. (2018)
1E 1547.0–5408	Outburst	15:50:54	−54:18:24	4.5	Coti Zelati et al. (2018)
SGR 0418+5729	Outburst	04:18:34	+57:32:23	2	Coti Zelati et al. (2018)
SGR 1833–0832	Outburst	18:33:46	−08:32:13	10	Coti Zelati et al. (2018)
Swift J1822.3–1606	Outburst	18:22:18	−16:04:27	1.6	Coti Zelati et al. (2018)
Swift J1834.9–0846	Outburst	18:34:53	−08:45:41	4.2	Coti Zelati et al. (2018)
1E 1048.1–5937	Outburst	10:50:09	−59:53:20	9	Coti Zelati et al. (2018)
SGR J1745–2900	Outburst	17:45:40	−29:00:30	8.3	Coti Zelati et al. (2018)
SGR 1935+2154 (FRB 200428) ^a	FRB	19:34:56	+21:53:48	4.4	Li et al. (2021)
SGR 1935+2154	IF/SB	Matsuoka et al. (2009), Sugawara et al. (2020)

Notes. As with the other variable classes, one listed object may correspond to multiple light curves within our X-ray phase space. To remain consistent with our discussion in Section 2.7, we categorize magnetar transience as either intermediate flare/short burst (IF/SB in the table) or outburst. Quiescent behavior is shown for the listed outbursts, with L_X taken from Olausen & Kaspi (2014).

^a SGR 1935+2154 is believed to be an FRB X-ray counterpart with a magnetar progenitor. For that reason, we include it with our sample of magnetar flares and outbursts. These data (both the IF/SB and FRB counterpart) are from the same burst forest in 2020 April for direct comparison. We adopt a distance of 4.4 kpc from Mereghetti et al. (2020).

Table A8
Cool Stellar Flares

Name	R.A.	Decl.	Distance (kpc)	References
UY Scl	00:14:46	−39:14:36	0.1372	Pye et al. (2015)
HD 1165	00:16:53	+81:39:49	0.0332	Pye et al. (2015)
HD 14716	02:16:04	−73:50:43	0.062	Pye et al. (2015)
CC Eri	02:34:23	−43:47:47	0.0116	Pye et al. (2015)
CD −53 544	02:41:47	−52:59:52	0.028	Pye et al. (2015)
SDSS J033815.04+002926.0	03:38:15	+00:29:26	0.7099	Pye et al. (2015)
V471 Tau	03:50:25	+17:14:47	0.0441	Pye et al. (2015)
2MASS J04072181–1210033	04:07:22	−12:10:03	0.3957	Pye et al. (2015)
V410 Tau	04:18:31	+28:27:16	0.0982	Pye et al. (2015)
T Tau	04:21:59	+19:32:06	0.1825	Pye et al. (2015)
HD 285845	04:31:25	+18:16:17	0.090	Pye et al. (2015)
HD 283810	04:40:09	+25:35:33	0.060	Pye et al. (2015)
HD 268974	05:05:27	−67:43:14	0.9174	Pye et al. (2015)
AB Dor	05:28:45	−65:26:55	0.0152	Pye et al. (2015)
SV Cam	06:41:19	+82:16:02	0.088	Pye et al. (2015)
pi.01 UMa	08:39:12	+65:01:15	0.0144	Pye et al. (2015)
2MASS J13141103–1620235	13:14:11	−16:20:24	0.5161	Pye et al. (2015)
1RXS J231628.7+790531	23:16:31	+79:05:36	0.055	Pye et al. (2015)

Note. As with the progenitors of other classes of recurrent outburst, individual flares are shown separately in our X-ray phase space, so some of the objects listed may correspond to a number of unique light curves.

Table A9
X-Ray Binary Outbursts and Ultraluminous X-Ray Sources

Name	Type	R.A.	Decl.	Distance (kpc)	Reference
4U 0352–309 (X Persei)	HMXRB	03:55:23	+31:02:45	1	La Palombara & Mereghetti (2007)
XMMU J004243.6+412519	ULX	00:42:44	+41:25:19	778	Middleton et al. (2013)
RX J0209.6–7427	HMXRB	02:09:34	–74:27:12	55	Vasilopoulos et al. (2020b)
PSR J1023+0038 ^a	LMXRB	10:23:48	+00:38:41	1.37	Bogdanov et al. (2015)
IGR J01217–7257 (SXP 2.16)	HMXRB	01:21:41	–72:57:22	62	Boon et al. (2017), Vasilopoulos et al. (2017a)
SXP 15.6	HMXRB	00:48:55	–73:49:46	62	Vasilopoulos et al. (2017b)
CG X-1	ULX	14:13:12	–65:20:14	4200	Qiu et al. (2019)
M51 ULX-7	ULX	13:30:01	+47:13:44	8580	Vasilopoulos et al. (2020a)
NGC 925 ULX-3	ULX	02:27:20	+33:34:13	9560	Earnshaw et al. (2020)
Aql X-1 ^b	LMXRB	19:11:16	+00:35:06	~5	López-Navas et al. (2020)
GX 339-4 ^b	LMXRB	17:02:49	–48:47:23	8	Kong et al. (2000), Corbel et al. (2013)
MAXI J1659–152	LMXRB	16:59:02	–15:15:29	6	Jonker et al. (2012)
4U J1907+09	HMXRB	19:09:41	+09:48:25	5	Ferrigno et al. (2022)
IGR J16393–4643	HMXRB	16:39:06	–46:42:14	12	Ferrigno et al. (2022)
IGR J17503–2636	HMXRB	17:50:18	–26:36:17	10	Ferrigno et al. (2022)
IGR J19140+0951	HMXRB	19:14:04	+09:52:58	2.8	Ferrigno et al. (2022)
Swift J0243.6+6124	HMXRB	02:43:40	+61:26:04	7	Wilson-Hodge et al. (2018), Chatzis et al. (2022)
RX J0520.5–6932	HMXRB	05:20:31	–69:31:55	50	Vasilopoulos et al. (2014)
SMC X-2	HMXRB	00:54:33	–73:41:01	62	Lutovinov et al. (2017)
SMC X-3	HMXRB	00:52:06	–72:26:04	62	Koliopanos & Vasilopoulos (2018)
XMMU J053108.3–690923	HMXRB	05:31:08	–69:09:24	50	Vasilopoulos et al. (2018), Maitra et al. (2021)
XTE J1859+226	LMXRB	18:58:42	+22:39:29	6.3	Hameury et al. (2003), Gallo et al. (2008)
GS 2023+338	LMXRB	20:24:04	+33:52:02	3.5	Kong et al. (2000)
4U 1630–47	LMXRB	16:34:02	–47:23:35	10	Kong et al. (2000)
CXOGLB J173617.6–444416	LMXRB	17:36:18	–44:44:17	9.9	Maxwell et al. (2012)
CXOGLB J173616.9–444409	LMXRB	17:36:17	–44:44:10	9.9	Maxwell et al. (2012)
CXOGLB J173617.3–444408	LMXRB	17:36:17	–44:44:08	9.9	Maxwell et al. (2012)
CXOGLB J173618.1–444359	LMXRB	17:36:18	–44:43:59	9.9	Maxwell et al. (2012)
CXOGLB J173617.5–444357	LMXRB	17:36:18	–44:43:57	9.9	Maxwell et al. (2012)
IGR J17544–2619	HMXRB	17:54:25	–26:19:53	3.5, 3.6	in’t Zand (2005), Sidoli et al. (2008)
IGR J08408–4503	HMXRB	08:40:48	–45:03:32	2.7	Leyder et al. (2007)
IGR J16479–4514	HMXRB	16:48:07	–45:12:07	4.9	Sidoli et al. (2008)
XTE J1739–302	HMXRB	17:39:12	–30:20:38	2.7	Sidoli et al. (2008)
IGR J18410–0535	HMXRB	18:41:00	–05:35:46	5	Sidoli et al. (2008)
CI Cam ^c	ULX	04:19:42	+55:59:58	1–10	Bartlett et al. (2019)

Notes. Objects with light curves shown in the X-ray phase space are above the horizontal line. Below the line, we list objects for which we show the quiescent behavior. As with other variable phenomena that show recurrent outbursts and flares, some objects may correspond to a number of unique light curves.

^a These data are not shared in the GitHub repository.

^b The light curves *and* quiescent behavior of Aql X-1 and GX 339-4 are shown in the X-ray phase space.

^c We note that CI Cam is a ULX as long as it is at a distance >8 kpc.

Table A10
Unclassified X-Ray Sources

Name	R.A.	Decl.	z	Distance (kpc)	References
XRT 000519	12:25:32	+13:03:59	0.23–1.5	1.62×10^4 1.1×10^6 1.11×10^7	Jonker et al. (2013)
XRT 110103 ^a	14:08:29	–27:03:29	...	9.49×10^4	Glennie et al. (2015)
XRT 120830 ^a	23:52:12	–46:43:43	...	0.08	Glennie et al. (2015)
Source 1	12:42:51	+02:38:35	...	1.43×10^4	Irwin et al. (2016)
Source 2	13:25:53	–43:05:46	...	3.8×10^3	Irwin et al. (2016)
CDF-S XT1 ^b	03:32:39	–27:51:34	0.3–2.23	1.6×10^6 1.81×10^7	Bauer et al. (2017)
CDF-S XT2	03:32:18	–27:52:24	0.738	4.68×10^6	Xue et al. (2019)
EXMM 023135.0-603743	02:31:35	–60:37:43	0.092	4.35×10^5	Novara et al. (2020)

Notes.

^a These data are digitized (Rohatgi 2019) and so are not included in the GitHub repository of light curves from this paper.

^b See also Quirola-Vásquez et al. (2022, 2023) for data and analysis.

Appendix B The True Observer’s Phase Space: Flux versus Duration

While the luminosity X-ray phase space is very instructive for understanding which physical phenomena are poorly captured by current instruments, it does little to reinforce the role that instrument sensitivity plays in determining which phenomena are detected. We show a purely observational duration–flux phase space in Figure 11.

Future missions will improve substantially on current sensitivity limits. This will open up an innately new area of the low-luminosity parameter space, significantly extending the depth out to which known classes of transients can be detected

and potentially revealing the existence of yet-unknown intrinsically faint signals.

Appendix C The Schematic DLPS

In addition to the phase space plots that are populated with real light curves, we offer a schematic version of the DLPS in Figure 12. We determine the bounds of the colored blocks based on the specific location of our collected light curves and use these regions as a guide to generate focused panels that show each (sub)class of transient in greater detail, rather than in the broader context of other signals in the DLPS.

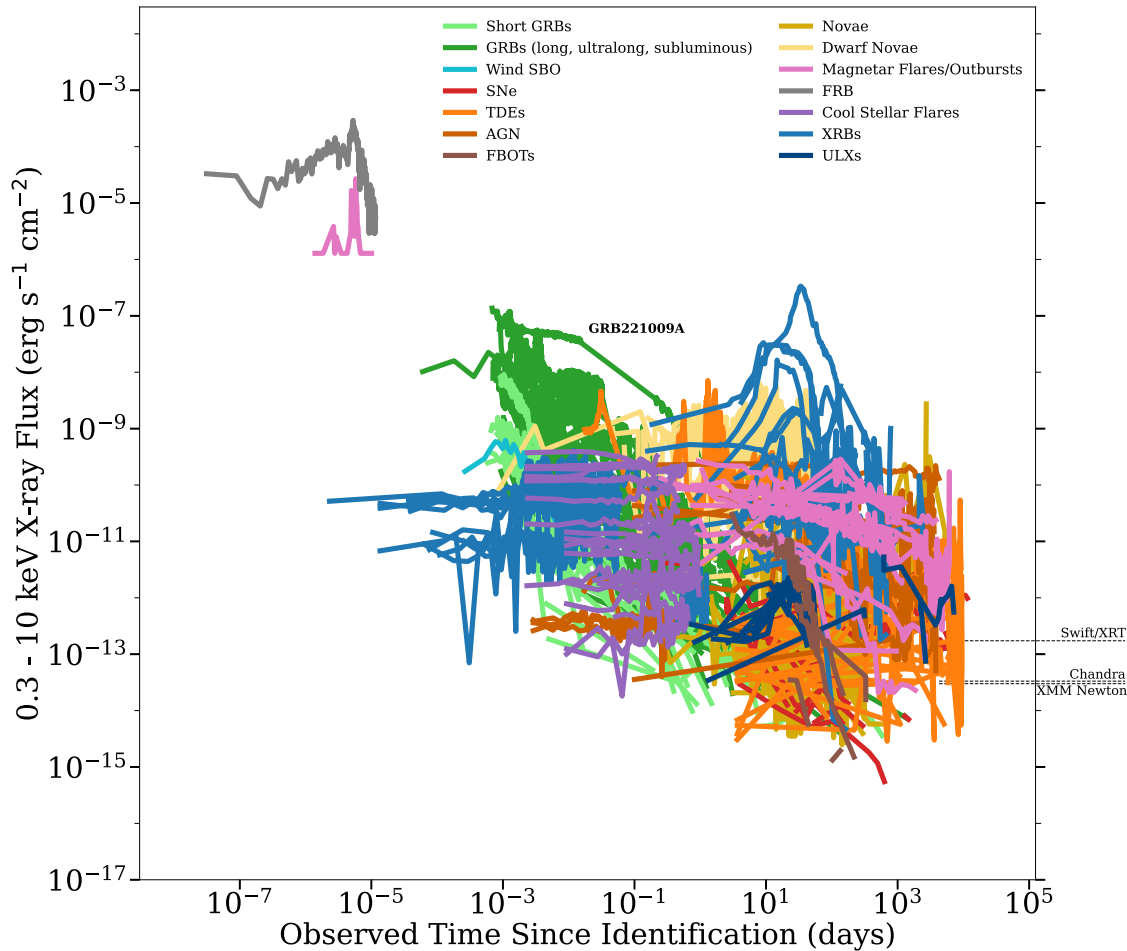


Figure 11. The duration–flux phase space of X-ray transient and variable phenomena. To demonstrate the limitations of current observatories, we mark the 0.3–10 keV flux limit for a handful of instruments, assuming a 1 ks integration time.

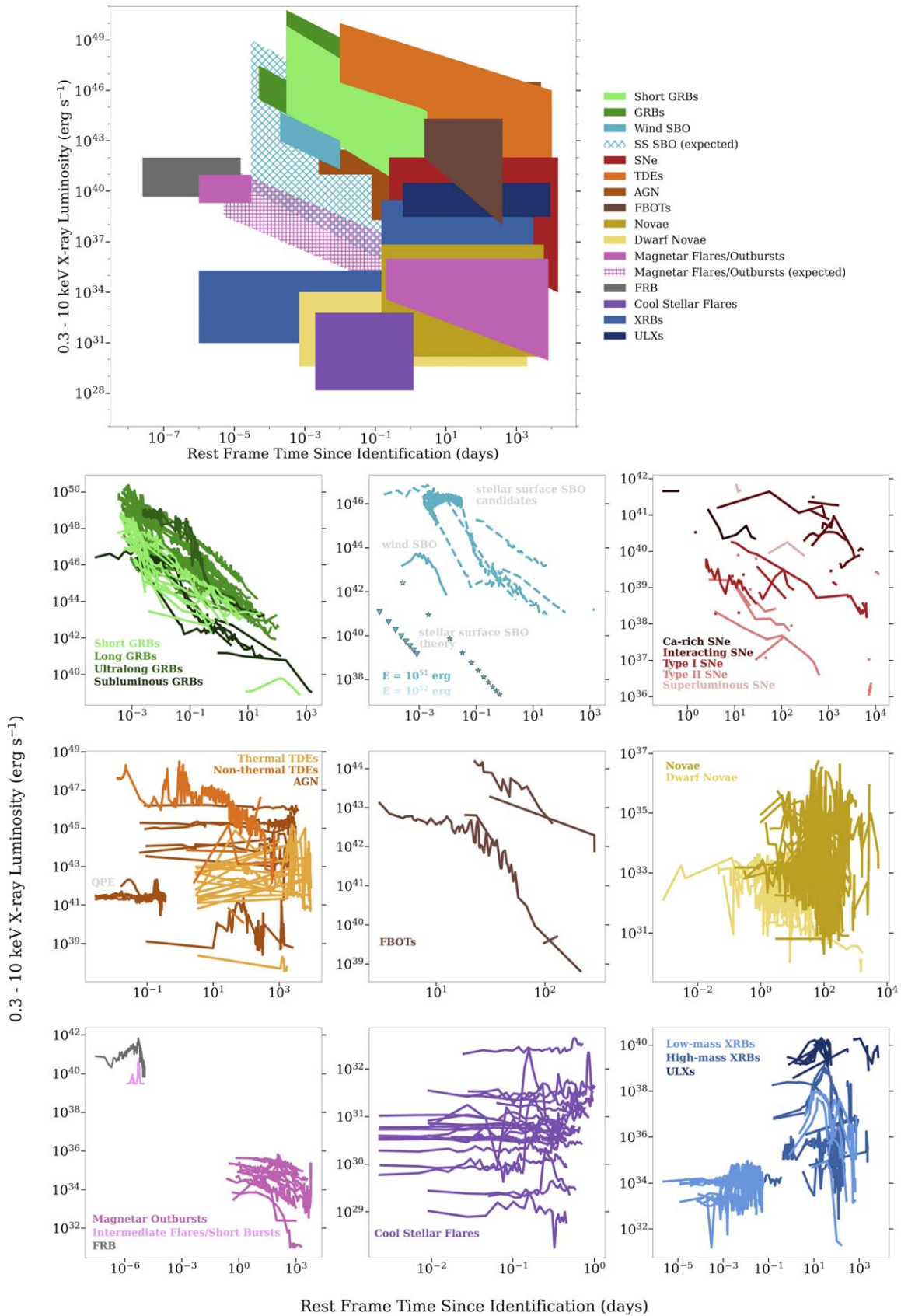













Figure 12. Top: a schematic illustration of the DLPS. Colored blocks cover the region where light curves of that class exist in the DLPS. The crosshatched blocks represent where we expect events of a particular class but have a paucity of observations (for SBOs, we include in this the region of the DLPS where we have *candidate* stellar surface SBOs). Bottom: an additional view of the DLPS, which emphasizes the phase space of individual classes of transient rather than their position in the larger transient phase space. We note that the lower panels are all scaled individually in duration and luminosity.

ORCID iDs

Ava Polzin  <https://orcid.org/0000-0002-5283-933X>
 Raffaella Margutti  <https://orcid.org/0000-0003-4768-7586>
 Deanne L. Coppejans  <https://orcid.org/0000-0001-5126-6237>
 Katie Auchettl  <https://orcid.org/0000-0002-4449-9152>
 Kim L. Page  <https://orcid.org/0000-0001-5624-2613>
 Georgios Vasilopoulos  <https://orcid.org/0000-0003-3902-3915>
 Joe S. Bright  <https://orcid.org/0000-0002-7735-5796>
 Paolo Esposito  <https://orcid.org/0000-0003-4849-5092>
 Peter K. G. Williams  <https://orcid.org/0000-0003-3734-3587>
 Koji Mukai  <https://orcid.org/0000-0002-8286-8094>
 Edo Berger  <https://orcid.org/0000-0002-9392-9681>

References

- Abbott, B. P., Abbott, R., Abbott, T. D., et al. 2017, *ApJL*, **848**, L12
 Alexander, K. D., van Velzen, S., Horesh, A., & Zauderer, B. A. 2020, *SSRv*, **216**, 81
 Alp, D., & Larsson, J. 2020, *ApJ*, **896**, 39
 Amati, L., O'Brien, P. T., Götz, D., et al. 2021, *ExA*, **52**, 183
 Angelini, L., & Verbunt, F. 1989, *MNRAS*, **238**, 697
 Arcavi, I., Wolf, W. M., Howell, D. A., et al. 2016, *ApJ*, **819**, 35
 Arzoumanian, Z., Gendreau, K. C., Baker, C. L., et al. 2014, *Proc. SPIE*, **9144**, 914420
 Astropy Collaboration, Price-Whelan, A. M., Sipőcz, B. M., et al. 2018, *AJ*, **156**, 123
 Astropy Collaboration, Robitaille, T. P., Tollerud, E. J., et al. 2013, *A&A*, **558**, A33
 Auchettl, K., Guillochon, J., & Ramirez-Ruiz, E. 2017, *ApJ*, **838**, 149
 Auchettl, K., Ramirez-Ruiz, E., & Guillochon, J. 2018, *ApJ*, **852**, 37
 Aydi, E., Orío, M., Beardmore, A. P., et al. 2018, *MNRAS*, **480**, 572
 Balberg, S., & Loeb, A. 2011, *MNRAS*, **414**, 1715
 Barcons, X., Barret, D., Decourchelle, A., et al. 2012, arXiv:1207.2745
 Bartlett, E. S., Clark, J. S., & Negueruela, I. 2019, *A&A*, **622**, A93
 Bauer, F. E., Dwarkadas, V. V., Brandt, W. N., et al. 2008, *ApJ*, **688**, 1210
 Bauer, F. E., Treister, E., Schawinski, K., et al. 2017, *MNRAS*, **467**, 4841
 Bietenholz, M. F., Bartel, N., Argo, M., et al. 2021, *ApJ*, **908**, 75
 Bochenek, C. D., Ravi, V., Belov, K. V., et al. 2020, *Natur*, **587**, 59
 Boella, G., Butler, R. C., Perola, G. C., et al. 1997, *A&AS*, **122**, 299
 Bogdanov, S., Archibald, A. M., Bassa, C., et al. 2015, *ApJ*, **806**, 148
 Boon, C. M., Bird, A. J., Coe, M. J., et al. 2017, *MNRAS*, **466**, 1149
 Bose, S., Dong, S., Kochanek, C. S., et al. 2021, *MNRAS*, **503**, 3472
 Brethauer, D., Margutti, R., Milisavljevic, D., et al. 2022, *ApJ*, **939**, 105
 Briel, U. G., Aschenbach, B., Hasinger, G., et al. 1996, *The ROSAT Users' Handbook* (Garching: Max Planck Institut)
 Bright, J. S., Fender, R. P., Motta, S. E., et al. 2018, *MNRAS*, **475**, 4011
 Bright, J. S., Margutti, R., Matthews, D., et al. 2022, *ApJ*, **926**, 112
 Brown, J. S., Holoien, T. W. S., Auchettl, K., et al. 2017, *MNRAS*, **466**, 4904
 Burrows, D. N., Hill, J. E., Nousek, J. A., et al. 2005, *SSRv*, **120**, 165
 Byckling, K., Osborne, J. P., Wheatley, P. J., et al. 2009, *MNRAS*, **399**, 1576
 Campana, S., Mangano, V., Blustin, A. J., et al. 2006, *Natur*, **442**, 1008
 Carter, B., & Luminet, J. P. 1982, *Natur*, **296**, 211
 Carter, B., & Luminet, J. P. 1983, *A&A*, **121**, 97
 Chakraborti, S., Ray, A., Smith, R., et al. 2013, *ApJ*, **774**, 30
 Chakraborti, S., Ray, A., Smith, R., et al. 2016, *ApJ*, **817**, 22
 Chandra, P., Chevalier, R. A., Chugai, N., Fransson, C., & Soderberg, A. M. 2015, *ApJ*, **810**, 32
 Chandra, P., Dwarkadas, V. V., Ray, A., Immler, S., & Pooley, D. 2009, *ApJ*, **699**, 388
 Chandra X-ray Center Chandra Project Science MSFC Chandra IPI Teams 2021, *The Chandra Proposers' Observatory Guide*, Tech. Rep. 24
 Chatzis, M., Petropoulou, M., & Vasilopoulos, G. 2022, *MNRAS*, **509**, 2532
 Chen, G., Ravi, V., & Lu, W. 2020, *ApJ*, **897**, 146
 Chesneau, O., Banerjee, D. P. K., Millour, F., et al. 2008, *A&A*, **487**, 223
 Chevalier, R. A., & Fransson, C. 2017, in *Handbook of Supernovae*, ed. A. W. Alsabti & P. Murdin (Cham: Springer)
 Coppejans, D. L., Margutti, R., Terreran, G., et al. 2020, *ApJL*, **895**, L23
 Corbel, S., Coriat, M., Brocksopp, C., et al. 2013, *MNRAS*, **428**, 2500
 Coti Zelati, F., Rea, N., Pons, J. A., Campana, S., & Esposito, P. 2018, *MNRAS*, **474**, 961
 Darnley, M. J., Ribeiro, V. A. R. M., Bode, M. F., & Munari, U. 2011, *A&A*, **530**, A70
 De Luca, A., Salvaterra, R., Belfiore, A., et al. 2021, *A&A*, **650**, A167
 de Ugarte Postigo, A., Izzo, L., Pugliese, G., et al. 2022, *GCN*, **32648**, 1
 Dong, F. A. & CHIME/FRB Collaboration 2022, *ATel*, **15681**, 1
 Drout, M. R., Chornock, R., Soderberg, A. M., et al. 2014, *ApJ*, **794**, 23
 Dwarkadas, V. V., & Gruszko, J. 2012, *MNRAS*, **419**, 1515
 Eappachen, D., Jonker, P. G., Fraser, M., et al. 2022, *MNRAS*, **514**, 302
 Earnshaw, H. P., Heida, M., Brightman, M., et al. 2020, *ApJ*, **891**, 153
 Eftekhari, T., Berger, E., Metzger, B. D., et al. 2022, *ApJ*, **935**, 16
 Esposito, P., De Luca, A., Turolla, R., et al. 2019, *A&A*, **626**, A19
 Esposito, P., Rea, N., & Israel, G. L. 2021, in *Timing Neutron Stars: Pulsations, Oscillations and Explosions*, ed. T. M. Belloni, M. Méndez, & C. Zhang (Berlin: Springer), 97
 Evans, P. A., Beardmore, A. P., Page, K. L., et al. 2007, *A&A*, **469**, 379
 Evans, P. A., Beardmore, A. P., Page, K. L., et al. 2009, *MNRAS*, **397**, 1177
 Evans, P. A., Page, K. L., Beardmore, A. P., et al. 2022, *MNRAS*, **518**, 174
 Evans, P. A., Page, K. L., Osborne, J. P., et al. 2020, *ApJS*, **247**, 54
 Ferrigno, C., Bozzo, E., & Romano, P. 2022, *A&A*, **664**, A99
 Fertig, D., Mukai, K., Nelson, T., & Cannizzo, J. K. 2011, *PASP*, **123**, 1054
 Fong, W., Berger, E., Margutti, R., & Zauderer, B. A. 2015, *ApJ*, **815**, 102
 Gallo, E., Homan, J., Jonker, P. G., & Tomsick, J. A. 2008, *ApJL*, **683**, L51
 Ghirlanda, G., & Salvaterra, R. 2022, *ApJ*, **932**, 10
 Giommi, P., Brandt, C. H., Barres de Almeida, U., et al. 2019, *A&A*, **631**, A116
 Glennie, A., Jonker, P. G., Fender, R. P., Nagayama, T., & Pretorius, M. L. 2015, *MNRAS*, **450**, 3765
 Greiner, J., Voges, W., Boller, T., & Hartmann, D. 1999, *A&AS*, **138**, 441
 Haberl, F., Geppert, U., Aschenbach, B., & Hasinger, G. 2006, *A&A*, **460**, 811
 Haberl, F., & Sturm, R. 2016, *A&A*, **586**, A81
 Hachisu, I., & Kato, M. 2018, *ApJS*, **237**, 4
 Hajela, A., Margutti, R., Alexander, K. D., et al. 2019, *ApJL*, **886**, L17
 Hajela, A., Margutti, R., Kathirgamaraju, A., et al. 2020, *RNAAS*, **4**, 68
 Hameury, J. M., Barret, D., Lasota, J. P., et al. 2003, *A&A*, **399**, 631
 Hancock, P. J., Anderson, G. E., Williams, A., et al. 2019, *PASA*, **36**, e046
 Harris, C. R., Millman, K. J., van der Walt, S. J., et al. 2020, *Natur*, **585**, 357
 Heinke, C. O., Bahramian, A., Degenaar, N., & Wijnands, R. 2015, *MNRAS*, **447**, 3034
 Heng, K., Haberl, F., Aschenbach, B., & Hasinger, G. 2008, *ApJ*, **676**, 361
 Ho, A. Y. Q., Margalit, B., Bremer, M., et al. 2022, *ApJ*, **932**, 116
 Ho, A. Y. Q., Perley, D. A., Gal-Yam, A., et al. 2021, *ApJ*, **949**, 120
 Holoien, T. W. S., Brown, J. S., Auchettl, K., et al. 2018, *MNRAS*, **480**, 5689
 Holoien, T. W. S., Vallety, P. J., Auchettl, K., et al. 2019, *ApJ*, **883**, 111
 Hunter, J. D. 2007, *CSE*, **9**, 90
 Hurley, K., Boggs, S. E., Smith, D. M., et al. 2005, *Natur*, **434**, 1098
 Immler, S. 2010, *ATel*, **2478**, 1
 Immler, S., Brown, P. J., Filippenko, A. V., & Pooley, D. 2007a, *ATel*, **1290**, 1
 Immler, S., Brown, P. J., Milne, P., et al. 2007b, *ApJ*, **664**, 435
 Immler, S., Li, B., Yang, Y., & Wilson, A. 2007c, *CBET*, **828**, 1
 Immler, S., Milne, P., & Pooley, D. 2010, *ATel*, **3012**, 1
 Immler, S., Modjaz, M., Landsman, W., et al. 2008, *ApJL*, **674**, L85
 Immler, S., & Pooley, D. 2007, *ATel*, **1004**, 1
 Immler, S., Pooley, D., & Brown, P. J. 2007d, *ATel*, **981**, 1
 Immler, S., Pooley, D., Brown, P. J., Li, W., & Filippenko, A. V. 2007e, *ATel*, **1284**, 1
 Immler, S., Pooley, D., Brown, P. J., & Milne, P. 2009, *ATel*, **1918**, 1
 Immler, S., & Russell, B. R. 2009, *ATel*, **2111**, 1
 in't Zand, J. J. M. 2005, *A&A*, **441**, L1
 Irwin, C. M., Linial, I., Nakar, E., Piran, T., & Sari, R. 2021, *MNRAS*, **508**, 5766
 Irwin, J. A., Maksym, W. P., Sivakoff, G. R., et al. 2016, *Natur*, **538**, 356
 Israel, G. L., Romano, P., Mangano, V., et al. 2008, *ApJ*, **685**, 1114
 Jacobson-Galán, W. V., Margutti, R., Kilpatrick, C. D., et al. 2020, *ApJ*, **898**, 166
 Jacobson-Galán, W. V., Venkatraman, P., Margutti, R., et al. 2022, *ApJ*, **932**, 58
 Jahoda, K., Swank, J. H., Giles, A. B., et al. 1996, *Proc. SPIE*, **2808**, 59
 Jansen, F., Lumb, D., Altieri, B., et al. 2001, *A&A*, **365**, L1
 Jonker, P. G., Glennie, A., Heida, M., et al. 2013, *ApJ*, **779**, 14
 Jonker, P. G., Miller-Jones, J. C. A., Homan, J., et al. 2012, *MNRAS*, **423**, 3308
 Kantharia, N. G. 2017, arXiv:1703.04087
 Koliopoulos, F., & Vasilopoulos, G. 2018, *A&A*, **614**, A23
 Komossa, S. 2015, *JHEAp*, **7**, 148

- Kong, A. K. H., Kuulkers, E., Charles, P. A., & Homer, L. 2000, *MNRAS*, **312**, L49
- Kouveliotou, C., Meegan, C. A., Fishman, G. J., et al. 1993, *ApJL*, **413**, L101
- Kouveliotou, C., Woosley, S. E., Patel, S. K., et al. 2004, *ApJ*, **608**, 872
- Kulkarni, S. R. 2012, arXiv:1202.2381
- La Palombara, N., & Mereghetti, S. 2007, *A&A*, **474**, 137
- Levan, A. J., Tanvir, N. R., Starling, R. L. C., et al. 2014, *ApJ*, **781**, 13
- Leyder, J. C., Walter, R., Lazos, M., Masetti, N., & Produit, N. 2007, *A&A*, **465**, L35
- Li, C. K., Lin, L., Xiong, S. L., et al. 2021, *NatAs*, **5**, 378
- Li, K.-L., Hamsch, F.-J., Munari, U., et al. 2020a, *ApJ*, **905**, 114
- Li, K. L., & Pun, C. S. J. 2011, arXiv:1109.0981
- Li, X., Li, X., Tan, Y., et al. 2020b, *JHEAp*, **27**, 64
- Linford, J. D., Chomiuk, L., Nelson, T., et al. 2017, *ApJ*, **842**, 73
- López-Navas, E., Degenaar, N., Parikh, A. S., Hernández Santisteban, J. V., & van den Eijnden, J. 2020, *MNRAS*, **493**, 940
- Lorimer, D. R., Bailes, M., McLaughlin, M. A., Narkevic, D. J., & Crawford, F. 2007, *Sci*, **318**, 777
- Lutovinov, A. A., Tsygankov, S. S., Krivonos, R. A., Molkov, S. V., & Poutanen, J. 2017, *ApJ*, **834**, 209
- Maitra, C., Haberl, F., Vasilopoulos, G., et al. 2021, *A&A*, **647**, A8
- Mangano, V., Burrows, D. N., Sbarufatti, B., & Cannizzo, J. K. 2016, *ApJ*, **817**, 103
- Margutti, R., & Chornock, R. 2021, *ARA&A*, **59**, 155
- Margutti, R., Metzger, B. D., Chornock, R., et al. 2019, *ApJ*, **872**, 18
- Margutti, R., Soderberg, A., & Milisavljevic, D. 2013, ATel, **5106**, 1
- Matsuoka, M., Kawasaki, K., Ueno, S., et al. 2009, *PASJ*, **61**, 999
- Matthews, D., Brethauer, D., Margutti, R., et al. 2022, *TNSAN*, **218**, 1
- Matthews, D., & Margutti, R. 2023, *TNSAN*, **159**, 1
- Maxwell, J. E., Lugger, P. M., Cohn, H. N., et al. 2012, *ApJ*, **756**, 147
- Mazzali, P. A., Valentí, S., Della Valle, M., et al. 2008, *Sci*, **321**, 1185
- McGowan, K. E., Priedhorsky, W. C., & Trudolyubov, S. P. 2004, *ApJ*, **601**, 1100
- McKinney, W. 2010, in SciPy Proc. 9th Python in Science Conf., ed. S. van der Walt & J. Millman, 56
- Meidinger, N. 2018, *CoSka*, **48**, 498
- Mereghetti, S., Savchenko, V., Ferrigno, C., et al. 2020, *ApJL*, **898**, L29
- Merloni, A., Predehl, P., Becker, W., et al. 2012, arXiv:1209.3114
- Metzger, B. D., Williams, P. K. G., & Berger, E. 2015, *ApJ*, **806**, 224
- Middleton, M. J., Miller-Jones, J. C. A., Markoff, S., et al. 2013, *Natur*, **493**, 187
- Miller, J. M., Kaastra, J. S., Miller, M. C., et al. 2015, *Natur*, **526**, 542
- Miniutti, G., Saxton, R. D., Guidini, M., et al. 2019, *Natur*, **573**, 381
- Misra, K., Pooley, D., Chandra, P., et al. 2007, *MNRAS*, **381**, 280
- Miura, J., Tsujimoto, M., Tsuboi, Y., et al. 2008, *PASJ*, **60**, S49
- Mong, Y.-L., & Ng, C.-Y. 2018, *ApJ*, **852**, 86
- Mukai, K. 1993, *Legacy*, **3**, 21
- Mukai, K. 2017, *PASP*, **129**, 062001
- Mukai, K., Orío, M., & Della Valle, M. 2008, *ApJ*, **677**, 1248
- Munari, U., Ribeiro, V. A. R. M., Bode, M. F., & Saguner, T. 2011, *MNRAS*, **410**, 525
- Mushotzky, R. 2018, *Proc. SPIE*, **10699**, 1069929
- Nakar, E. 2012, *ApJ*, **747**, 88
- Nakar, E. 2015, *ApJ*, **807**, 172
- Nakar, E. 2020, *PhR*, **886**, 1
- Nakar, E., & Sari, R. 2010, *ApJ*, **725**, 904
- Neustroev, V. V., Page, K. L., Kuulkers, E., et al. 2018, *A&A*, **611**, A13
- Nisenoff, A., Dwarkadas, V. V., & Ross, M. C. 2020, *RNAAS*, **4**, 195
- Norris, J. P. 2003, in AIP Conf. Ser. 686, The Astrophysics of Gravitational Wave Sources, ed. J. M. Centrella (Melville, NY: AIP), 74
- Novara, G., Esposito, P., Tiengo, A., et al. 2020, *ApJ*, **898**, 37
- O'Brien, P. T., & Smartt, S. J. 2013, *RSPTA*, **371**, 20120498
- Olausen, S. A., & Kaspi, V. M. 2014, *ApJS*, **212**, 6
- Page, K. L., Beardmore, A. P., & Osborne, J. P. 2020, *AdSpR*, **66**, 1169
- Pala, A. F., Gänsicke, B. T., Breedt, E., et al. 2020, *MNRAS*, **494**, 3799
- pandas development team, T. 2020, pandas-dev/pandas: Pandas, v1.1.3, Zenodo, doi:10.5281/zenodo.4067057
- Pedregosa, F., Varoquaux, G., Gramfort, A., et al. 2011, *JMLR*, **12**, 2825
- Petroff, E., Hessels, J. W. T., & Lorimer, D. R. 2019, *A&ARv*, **27**, 4
- Petroff, E., Hessels, J. W. T., & Lorimer, D. R. 2022, *A&ARv*, **30**, 2
- Pian, E., Amati, L., Antonelli, L. A., et al. 2000, *ApJ*, **536**, 778
- Pietka, M., Fender, R. P., & Keane, E. F. 2015, *MNRAS*, **446**, 3687
- Pietrzyński, G., Graczyk, D., Gieren, W., et al. 2013, *Natur*, **495**, 76
- Pleunis, Z., Good, D. C., Kaspi, V. M., et al. 2021, *ApJ*, **923**, 1
- Poggiani, R. 2009, *NewA*, **14**, 4
- Polzin, A., Margutti, R., Coppejans, D. L., et al. 2023, X-rayLCs: Data and code from Polzin et al. (2023), v1.0, Zenodo, doi:10.5281/zenodo.8319602
- Pooley, D., Immler, S., & Filippenko, A. V. 2007, ATel, **1023**, 1
- Pooley, D., Lewin, W. H. G., Fox, D. W., et al. 2002, *ApJ*, **572**, 932
- Predehl, P., Andritschke, R., Arefiev, V., et al. 2021, *A&A*, **647**, A1
- Pursiainen, M., Childress, M., Smith, M., et al. 2018, *MNRAS*, **481**, 894
- Pye, J. P., Rosen, S., Fyfe, D., & Schröder, A. C. 2015, *A&A*, **581**, A28
- Qiu, Y., Soria, R., Wang, S., et al. 2019, *ApJ*, **877**, 57
- Quirola-Vásquez, J., Bauer, F. E., Jonker, P. G., et al. 2022, *A&A*, **663**, A168
- Quirola-Vásquez, J., Bauer, F. E., Jonker, P. G., et al. 2023, *A&A*, **675**, A44
- Raj, A., Ashok, N. M., Rudy, R. J., et al. 2015, *AJ*, **149**, 136
- Raj, A., Banerjee, D. P. K., & Ashok, N. M. 2013, *MNRAS*, **433**, 2657
- Ramsden, P., Lanning, D., Nicholl, M., & McGee, S. L. 2022, *MNRAS*, **515**, 1146
- Ray, P. S., Arzoumanian, Z., Ballantyne, D., et al. 2019, arXiv:1903.03035
- Rea, N., Borghese, A., Esposito, P., et al. 2016, *ApJL*, **828**, L13
- Rea, N., Esposito, P., Pons, J. A., et al. 2013, *ApJL*, **775**, L34
- Reig, P. 2011, *Ap&SS*, **332**, 1
- Rivera Sandoval, L. E., Maccarone, T. J., Corsi, A., et al. 2018, *MNRAS*, **480**, L146
- Rivera Sandoval, L. E., Maccarone, T. J., Corsi, A., et al. 2019, *MNRAS*, **484**, L7
- Rohatgi, A. 2019, WebPlotDigitizer (4.2), <https://automeris.io/WebPlotDigitizer>
- Roming, P. W. A., Pritchard, T. A., Brown, P. J., et al. 2009, *ApJL*, **704**, L118
- Ross, M., & Dwarkadas, V. V. 2017, *AJ*, **153**, 246
- Rouco Escorial, A., Fong, W.-f., Berger, E., et al. 2022, arXiv:2210.05695
- Russell, B. R., & Immler, S. 2010, ATel, **2389**, 1
- Russell, B. R., Immler, S., & Milne, P. 2010, ATel, **2618**, 1
- Russell, T. D., Miller-Jones, J. C. A., Sivakoff, G. R., et al. 2016, *MNRAS*, **460**, 3720
- Sazonov, S., Gilfanov, M., Medvedev, P., et al. 2021, *MNRAS*, **508**, 3820
- Sazonov, S. Y., Lutovinov, A. A., & Sunyaev, R. A. 2004, *Natur*, **430**, 646
- Schaefer, B. E. 2010, *ApJS*, **187**, 275
- Schaefer, B. E. 2018, *MNRAS*, **481**, 3033
- Schlegel, E. M. 2001, *ApJL*, **556**, L25
- Schlegel, E. M., & Ryder, S. 2002, IAU, **7913**, 1
- Schulze, S., Ho, A. Y. Q., Perley, D. A., Yan, L., & Fremling, C. 2022, *TNSAN*, **207**, 1
- Sidoli, L., Romano, P., Mangano, V., et al. 2008, *ApJ*, **687**, 1230
- Soderberg, A., Grindlay, J. E., Bloom, J. S., et al. 2009, arXiv:0902.3674
- Soderberg, A. M., Berger, E., Page, K. L., et al. 2008, *Natur*, **453**, 469
- Soderberg, A. M., Chevalier, R. A., Kulkarni, S. R., & Frail, D. A. 2006, *ApJ*, **651**, 1005
- Soderberg, A. M., Margutti, R., Zauderer, B. A., et al. 2012, *ApJ*, **752**, 78
- Soria, R., Pian, E., & Mazzali, P. A. 2004, *A&A*, **413**, 107
- Staley, T. D., Titterton, D. J., Fender, R. P., et al. 2013, *MNRAS*, **428**, 3114
- Stone, N. C., & Metzger, B. D. 2016, *MNRAS*, **455**, 859
- Sturm, R., Haberl, F., Aschenbach, B., & Hasinger, G. 2010, *A&A*, **515**, A5
- Sugawara, Y., Nakahira, S., Negro, H., et al. 2020, GCN, **27661**, 1
- Sugizaki, M. 2010, in The First Year of MAXI: Monitoring Variable X-ray Sources (Tokyo: MAXI/RIKEN), 14
- Svirski, G., & Nakar, E. 2014, *ApJL*, **788**, L14
- Tanaka, M., Tominaga, N., Morokuma, T., et al. 2016, *ApJ*, **819**, 5
- Tanaka, Y., Inoue, H., & Holt, S. S. 1994, *PASJ*, **46**, L37
- Tetarenko, B. E., Sivakoff, G. R., Heinke, C. O., & Gladstone, J. C. 2016, *ApJS*, **222**, 15
- The CHIME/FRB Collaboration, Andersen, B. Å. C., Bandura, K. Å. M., et al. 2020, *Natur*, **587**, 54
- The Lynx Team 2019, Lynx X-ray Observatory Concept Study Report, Tech. rep., Lynx Observatory
- Tozzi, P., Gilli, R., Mainieri, V., et al. 2006, *A&A*, **451**, 457
- Trümper, J. 1990, in IAU Coll., 115, High Resolution X-ray Spectroscopy of Cosmic Plasmas (Cambridge: Cambridge Univ. Press), 291
- Tsuboi, Y., Yamazaki, K., Sugawara, Y., et al. 2016, *PASJ*, **68**, 90
- Tsunemi, H., Tomida, H., Katayama, H., et al. 2010, *PASJ*, **62**, 1371
- Vasilopoulos, G., Haberl, F., & Maggi, P. 2017a, *MNRAS*, **470**, 1971
- Vasilopoulos, G., Haberl, F., Sturm, R., Maggi, P., & Udalski, A. 2014, *A&A*, **567**, A129
- Vasilopoulos, G., Lander, S. K., Koliopanos, F., & Bailyn, C. D. 2020a, *MNRAS*, **491**, 4949
- Vasilopoulos, G., Maitra, C., Haberl, F., Hatzidimitriou, D., & Petropoulou, M. 2018, *MNRAS*, **475**, 220
- Vasilopoulos, G., Ray, P. S., Gendreau, K. C., et al. 2020b, *MNRAS*, **494**, 5350

- Vasilopoulos, G., Zezas, A., Antoniou, V., & Haberl, F. 2017b, *MNRAS*, **470**, 4354
- Villar, V. A., Berger, E., Metzger, B. D., & Guillochon, J. 2017, *ApJ*, **849**, 70
- Virtanen, P., Gommers, R., Oliphant, T. E., et al. 2020, *NatMe*, **17**, 261
- Wang, C. W., Xiong, S. L., Zhang, Y. Q., et al. 2022, *ATel*, **15682**, 1
- Watson, D., Hjorth, J., Levan, A., et al. 2004, *ApJL*, **605**, L101
- Watson, M. G., Auguères, J. L., Ballet, J., et al. 2001, *A&A*, **365**, L51
- Wei, J., Cordier, B., Antier, S., et al. 2016, arXiv:1610.06892
- Weisskopf, M. C., Tananbaum, H. D., Van Speybroeck, L. P., & O'Dell, S. L. 2000, *Proc. SPIE*, **4012**, 2
- Wheatley, P. J., Mauche, C. W., & Mattei, J. A. 2003, *MNRAS*, **345**, 49
- Wilson-Hodge, C. A., Malacaria, C., Jenke, P. A., et al. 2018, *ApJ*, **863**, 9
- Worpel, H., Schwope, A. D., Traulsen, I., Mukai, K., & Ok, S. 2020, *A&A*, **639**, A17
- Xue, Y. Q., Zheng, X. C., Li, Y., et al. 2019, *Natur*, **568**, 198
- Yao, Y., Ho, A. Y. Q., Medvedev, P., et al. 2022, *ApJ*, **934**, 104
- Yao, Y., Ravi, V., Gezari, S., et al. 2023, *ApJL*, **955**, L6
- Yuan, W. 2017, in 7 years of MAXI: Monitoring X-ray Transients, ed. M. Serino et al. (Tokyo: MAXI/RIKEN), 247
- Zampieri, L., Mucciarelli, P., Pastorello, A., et al. 2005, *MNRAS*, **364**, 1419
- Zhang, S., Santangelo, A., Feroci, M., et al. 2019, *SCPMA*, **62**, 29502
- Zhang, S.-N., Li, T., Lu, F., et al. 2020, *SCPMA*, **63**, 249502